

MOLECULAR SIMULATIONS OF SOLID SURFACE
- POLYMER SOLUTION INTERFACES (AT
SEGMENTAL AND CHAIN SCALE)

By

RAVI KIRAN BALLAMUDI

A DISSERTATION PRESENTED TO THE GRAUATE SCHOOL OF THE
UNIVERSITY OF FLORIDA IN PARTIAL FULFILLMENT OF THE
REQUIREMENTS FOR THE DEGREE OF DOCTOR OF PHILOSOPHY

UNIVERSITY OF FLORIDA

1997

ACKNOWLEDGEMENTS

My experience in preparing for the Doctorate in Philosophy degree has been a unique blessing where I have discovered a great deal about my interests, skills and life. I owe a great debt to many unique individuals for this rich and joyous experience. First among them are my parents Sri B. V. Ramana and Smt. B. Amba Ramana whose consistent encouragement and love made this possible. I am deeply grateful to Professor Ioannis Bitsanis, my doctoral thesis advisor, for directing my research work while encouraging independent thought and a great degree of freedom.

My graduate education has been a rich and exciting experience where the lessons learnt are not trivial. My foremost thanks go to Professor Lewis Johns for the many stimulating and insightful discussions on many scientific and educational subjects and for agreeing to serve on my doctoral committee. I am deeply indebted to Professor Gar Hoflund for helping me see the purpose of education very early during my graduate studies.

The Engineering Research Center for Particle Science and Technology at University of Florida has broadened my perspective on many research problems. I thank Professor Brij Moudgil and all the people who made this center possible. Many thanks are due to the members of the Simulation, Modeling and Visualization group, where constructive criticism has helped improve my research work. Special thanks are due to Professors

Paul Fishwick, Sergei Obukhov, C.W. Park, Raj Rajagopalan and late Gerry Westermann-Clark for serving on my doctoral committee.

My life as a student has been enriched due to the indelible influence of many friends and relatives. I am grateful for the support of my sister Mrs. B. Hima Bindu and cousin Professor Sastry Pantula. The support of all my friends in the past several years, including Pia Gavino, Kostas Hrissagis, Natasha Hunte, Krishna Maruvada, Ivanova Narvaez, Alina Ruta, Sujatha Sugavanam, Joanne Thomatos, Adriana White, Jacqueline White and many others is deeply appreciated.

TABLE OF CONTENTS

ACKNOWLEDGEMENTS	ii
ABSTRACT.....	vi
1. INTRODUCTION	1
1.1 Motivation.....	1
1.2 Introduction to Solid-Polymer Interfaces.....	2
1.2.1 Proximal Interface.....	3
1.2.2 Distal Interface.....	4
1.3 Modeling Issues in Solid Particle-Polymer Interfaces.....	4
2. LITERATURE REVIEW	9
2.1 Studies of Oligomer Interfaces and Films	9
2.2 Studies of Solid-Polymer Solution Interfaces.....	14
2.2.1 Scaling Theory	17
2.2.2 SF Theory.....	17
2.2.3 Two Order Parameter Mean Field Theory of Semenov and coworkers	18
3. COMPUTER SIMULATION AND MODELING	21
3.1 Brief History	22
3.2 Tricks of the Trade.....	23
3.2.1 Periodic Boundaries	23
3.2.2 Nearest Neighbor Lists	23
3.3 Initial Configurations	24
3.3.1 Molecular Dynamics Studies	24
3.3.2 Monte Carlo Studies	25
4. SIMULATIONS OF ULTRA THIN FILMS OF N-OCTANE	27
4.1 Introduction.....	27
4.2 Molecular Model and Simulation Method.....	27
4.2.1 Introduction.....	27
4.2.2 Molecular Interactions	29
4.3 Data Acquisition and Data Analysis in Molecular Dynamics	32

4.4 System Description	34
4.4.1 Effect of Solid-Segment Affinity	34
4.4.2 Effect of Normal Pressure	35
4.5 Results and Discussion	36
4.5.1 Simulation Results	36
4.5.2 Discussion	41
4.5.3 Summary	46
4.6 Simulations at Constant Isotropic Pressure.....	47
4.6.1 Algorithm for Simulating Constant Isotropic Pressure.....	48
4.6.2 Integration of Equations of Motion.....	49
4.6.3 Results and Discussion	50
4.6.4 Conclusions.....	51
 5. SIMULATIONS OF SOLID PARTICLE-POLYMER SOLUTION INTERFACES ...	78
5.1 Introduction.....	78
5.2 Model Description	78
5.3 Methodology	80
5.3.1 Simple Lattice Monte Carlo Algorithm	81
5.3.2 Configurational Bias Monte Carlo Algorithm	81
5.4 Determination of Theta Solvent Conditions	83
5.5 System Description	85
5.6 Results and Discussion	86
5.6.1 Proximal Regime	90
5.6.2 Distal Regime.....	92
5.7 Summary and Conclusions	92
5.8 Future Directions	93
5.8.1 Particle-Bidisperse Polymer Solution Interface.....	94
5.8.2 Particle-Polyelectrolyte Solution Interface	94
 REFERENCES	111
 BIOGRAPHICAL SKETCH	118

Abstract of Dissertation Presented to the Graduate School
of the University of Florida in Partial Fulfillment of the
Requirements for the Degree of Doctor of Philosophy

MOLECULAR SIMULATIONS OF SOLID SURFACE - POLYMER SOLUTION
INTERFACES (AT SEGMENTAL AND CHAIN SCALE)

By

Ravi Kiran Ballamudi

May 1997

Chairman: Professor Ioannis Bitsanis

Major Department: Chemical Engineering

Investigations of solid surface and polymer solution interfaces constitute the theme of this doctoral research. Two important aspects of the solid-polymer interface problem have been studied. The first part studies the proximal interface. Here ultra-thin films of n-octane confined between geometrically flat surfaces are studied by molecular dynamics simulations. The role of surface energy and normal pressure are investigated. The results of this work show that upon increasing the solid surface-polymer segment energy ϵ_{sl} , the in-layer pair correlation function curve undergoes an abrupt transition as ϵ_{sl} crosses a threshold value. This change is accompanied by the cessation of translational and rotational diffusion. The molecules form ordered micro-crystalline domains above the threshold ϵ_{sl} value. These observations amount to a liquid to solid transition with the increase in the physisorption energy, without any aid from the topography of the solid

substrate. Increasing the normal pressure also results in a similar first order phase transition. These simulations show that highly adsorbing surfaces like mica, which is commonly used in Surface Force Apparatus experiments, are capable of solidifying a thin film of oligomers.

In the second part, interfaces of a solid particle and a dilute neutral polymer solution under theta conditions were simulated using Configurational Bias Monte Carlo methods. These simulations analyzed the conformational features of the chains of intermediate length ($N \leq 300$). Polymer chains adsorbed with collapsed conformations under dilute concentrations. Increasing the bulk concentration resulted in more chains adsorbing loosely on the surface with shorter trains and longer tails and loops. The two order parameter mean field theory of Semenov and coworkers and the scaling prediction of de Gennes were tested. The overall segment density profiles and the loop density profile decay with an exponent close to -2 in the proximal interface. The decay in the loop and tail segment profiles in the distal regime are exponential. The relatively minor deviations observed in the simulations from the theory are due to the fact that polymer chains that could be simulated with the methods currently employed may not yet be well within the long molecular weight range, where the scaling predictions might be expected to be followed closely.

CHAPTER 1

INTRODUCTION

Polymers in the present day are ubiquitous. In this dissertation we focus on researching the properties of linear homopolymer chains at solid interfaces. Understanding the properties of polymers at interfaces is very important in a multitude of applications such as nanotribology (hard disk coatings)¹, colloidal stabilization, polymer extrusion (manufacturing method for several polymer products, including the house hold trash bags)^{2,3}, flow through microporous media and enhanced oil recovery.

1.1 Motivation

There are several important industrial applications of physisorbed thin polymer films. Ultra thin film polymer coatings ($\sim 10^2 \text{\AA}$) are necessary for protecting the present day micro electronic devices like hard disks¹. Another very important application of polymers in the present day industry is as colloidal suspension stabilizers.

Colloidal suspensions consist of microscopic particles of micron or sub micron size and in which Brownian motion is ever present⁴. Examples of colloidal suspensions include paint, milk and cough syrup.

Keeping colloidal suspensions stable is of enormous industrial importance. Paint needs to be stable for easy application and uniform thickness of the coating. In the pharmaceutical industry keeping some drugs in stable suspension form is essential to ensure correct dosage. Suspensions are also a common occurrence in most chemical

industry processes such as paper and pulp, ceramics, oil production, pharmaceuticals, petrochemicals and biomedical engineering.

Particles in a colloidal suspension experience electrostatic and dispersive forces, and hydrodynamic forces under flow. The balance of attractive and repulsive forces between particles determines the final stability of the suspension. Figure 1.1 shows a schematic of forces between two colloidal particles. When the repulsive electrostatic forces dominate, the suspension remains stable. When the attractive van der Waal's forces dominate, the particles coagulate. The stability of a suspension can be influenced by either changing the existing forces or by introducing new forces. For instance, the electrostatic repulsion can be controlled by changing the pH of the solution.

One effective way of preventing colloidal coagulation is to introduce a steric barrier between particles. This is accomplished by coating the particle surfaces with polymer chains. Although polymers are widely used as suspension stabilizers in the industry, the mechanism is not yet fully understood. Understanding the interface between the colloidal particle surface and the polymer chains in solution is extremely important to design and tailor polymers that will be effective as concentrated suspension stabilizers.

1.2 Introduction to Solid-Polymer Interfaces

The interface between a solid particle and long polymer chains can be divided into the proximal, intermediate and distal interfaces, as shown in the schematic in figure 1.2. In the proximal interface the effects of the short range forces between the polymer segments and the surface of the particle are important. The intermediate regime is characterized by a strongly universal concentration profile, independent of the bulk concentration. The

distal interface consists of the outer region into which the adsorbed chain extends. These regimes are clearly distinguishable for extremely long chains ($N > 10^5$; $MW > 10^7$). For long chains ($10^3 < N < 10^4$; $10^5 < MW < 10^6$) the proximal and intermediate regimes may not be clearly distinguishable. In such cases, the interface is considered to be made up of just the proximal and distal regimes. Our study examines the polymer segment behavior in both the proximal and distal interfaces.

The conformations of the polymer chain next to the solid surface can be described in terms of tails, trains and loops (see Figure 1.3). Trains are sequences of segments that mainly constitute the proximal interface. Loops are segment sequences that connect consecutive trains. Tails are free ends of the chain. An adsorbed polymer chain may have either 0, 1 or 2 tails. The loops and tails make up the intermediate and distal interface. In this work we are concerned with either very short ($N=8$) chains or with chains of intermediate length ($N \leq 300$).

1.2.1 Proximal Interface

The concentration of the polymer segments in the proximal interface is mostly due to trains. This concentration depends upon the solid surface adhesive energy, polymer chain length, solvent conditions and concentration of polymer in bulk. For particle surfaces that have an attractive energy close to one unit of thermal energy, the polymer segment density in the proximal interface is melt-like.

It is known that the average polymer train size at solid-polymer melt interfaces reaches an asymptotic limit very quickly with increasing chain length⁵⁻⁷. This proximal interface is hence similar to a solid-short chain polymer interface. The structural features

of these adsorbed segments in the proximal interface have a strong influence on the behavior of the overall chain. If the surface segments are solid-like, the overall chain mobility is severely impeded, while mobile surface segments allow much greater kinetic and conformational freedom to the adsorbed chains. The structure and dynamics of the proximal interface can be investigated qualitatively by studying a solid surface-short chain polymer interface.

In the first part of this thesis, using molecular dynamics, solid surface-short alkane chain interfaces are simulated. We investigate the influence of solid-segment interaction energy and thermodynamic conditions (pressure and temperature) on the structural characteristics of the proximal layer.

1.2.2 Distal Interface

The loops and tails constitute the distal interface. The distal layer is responsible for the steric barrier between two approaching colloidal particles. The characteristics of the loops and tails can be examined by studying long polymer chain conformations adsorbed on solid particle surfaces. In the second part of the thesis, the long chain polymer features are studied using Monte Carlo methods.

1.3 Modeling Issues in Solid Particle-Polymer Interfaces

Modeling the solid particle-polymer chain interfaces requires careful attention. While the short scale segmental features of polymer chains are critically dependent on the monomer architecture, long polymer chains obey universal laws. Long chains can be described using simple models, where a group of chemical monomer units is treated as

one "segment." For short chains, it is necessary to consider more refined and accurate models that take the molecular architecture and chemistry into consideration.

Hence in the first part of this thesis, the proximal interface is studied using a detailed model for n-octane with various potentials governing the short scale features. In the second part of the thesis, where the goal is to understand the global features of long polymer chains at interfaces, a cubic lattice model is employed.

The rest of this manuscript is organized as follows. In chapter 2, the existing body of relevant literature is reviewed. The first part of the review examines the solid-oligomer melt interfaces. The second part of the review focuses on the solid surface-polymer chain solution interfaces. Some of the existing theories are discussed. Chapter 3 contains a discussion of computer simulations of systems similar to those studied here. A general discussion of important issues while simulating solid-polymer interfaces is given. Chapter 4 begins with a discussion of the modeling and simulation of ultra thin films of n-octane. Next, the results of Molecular Dynamics simulations investigating the effect of solid surface energy and pressure are elaborated. Chapter 5 deals with the second part of our research studying solid particle-dilute polymer solution interfaces. Modeling and simulation aspects of the system of interest are discussed followed by an analysis of the data. Finally, the future directions of this research are suggested.

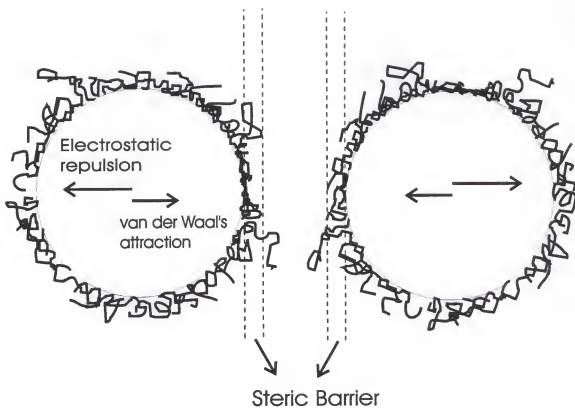


Figure 1.1. Schematic of two colloidal particles with adsorbed polymer chains. The particles experience electrostatic repulsion, van der Waal's attraction, hydrodynamic and steric forces.

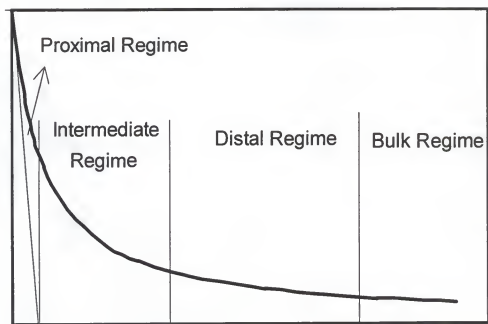


Figure 1.2. Schematic of the segment density profile of a solid particle surface and polymer chain interface. The different interfacial regimes are shown.

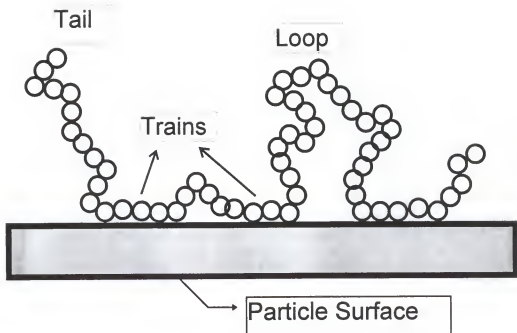


Figure 1.3. Schematic of a physisorbing solid surface and a polymer chain. The conformations of the polymer chain constitutes of tails, trains and loops.

CHAPTER 2

LITERATURE REVIEW

There is a wide spectrum of challenging and difficult problems related to the physics of linear flexible macromolecules. The static properties of these chains have been summarized in Flory's book⁸. Polymers at interfaces and in solution have been the focus of many theoretical, experimental and computational studies in the past few decades⁹⁻¹².

Studies of Oligomer Interfaces and Films

Oligomers are short chains of polymers ($N \ll 10^3$). Oligomers next to a solid surface configure themselves differently from the molecules far removed from the solid surface. The presence of a solid surface next to oligomeric chains influences their behavior as the solid surface alters their mobility, conformation and the relaxation times. Consequently, the material properties of interfacial and ultra-thin films are altered at the molecular level. Hence, the structure and the rheological properties of such films of oligomeric fluids can be drastically different from their bulk properties.

Long polymer chain conformations next to a solid surface were investigated by several computer simulations^{4-7,13-17}. The theory of long chain polymer conformations at a solid-polymer melt interface has a long history^{13, 14, 18-21}. Polymer chain conformations at a solid-melt interface consist of tails, trains and loops. Trains are sub-chains that lie flat on the solid surface and loops are sub-chains that connect two consecutive trains. Tails are ends of the polymer chain that do not lie flat on the solid surface. The region of the

solid-polymer melt interface, that contains trains is referred to as the proximal interface and the region over which the loops and tails extend is identified as the distal interface.

The mobility of whole polymer chains is critically dependent on the mobility of segments in the proximal interface. If the surface segments are solid-like, the trains are irreversibly adsorbed and the overall chain mobility is severely impeded, thus dramatically effecting the distal interface dynamics. Mobile surface segments allow much greater kinetic and conformational freedom to the adsorbed chains. For strongly adsorbing surfaces (mica, metal oxides, metals), the immobilization of segments inside the proximal interface is suggested by some indirect experiments. Before examining the experimental evidence it is important to understand that the dynamics of short chain polymers next to a solid surface closely mimic the dynamics of segments in the proximal interface between solids and long chain polymer-melts. The size distributions of trains and loops as a function of the polymer chain length has been the objective of simulation and theoretical studies^{7, 18-21}. The average length of trains reaches a plateau of about 5 cubic lattice segments, with increasing chain length. The proximal interface can now be viewed as consisting of several short chain polymer molecules and the dynamics of the short chain molecules in the first layer is very similar to the long polymer chain dynamics in the proximal interface.

Much of the evidence pointing towards the immobilization of first layer polymer molecules was supplied by experiments on thin polymer films using the Surface Force Apparatus (SFA) developed by Israelachvili²³. Since the development of SFA and its subsequent modification²⁴⁻²⁸ for simultaneous shear and normal force measurements,

several shear and squeezing flow studies were performed on thin films of polymer melts. A number of SFA experiments measured strong repulsive forces between surfaces confining thin polymer melts when the surfaces were separated by a distance of $4R_g$ ^{26, 29-31}. Such forces could exist only if the molecules were irreversibly adsorbed on the surface, as mobile chains would not have caused the appearance of equilibrium forces in films of thickness comparable to R_g ^{13, 14, 32}. However, under certain conditions when the system is composed of random heteropolymers, the three body interaction term could become important and the confining surfaces might experience a net attractive force³³. The above SFA experiments provide indirect evidence of the immobilization of the segments in the proximal interface. Shear flow experiments on short chain polymer films that are 4-5 segmental diameters wide reported that the film would not flow until a "critical" shear stress was applied^{25, 27, 28}. Also, Scanning Tunneling Microscopy (STM) experiments on oligomer monolayers deposited on metal surfaces have detected highly ordered domains (microcrystallites)^{34, 35}. Squeezing flow experiments on dense micellar systems reported a stepwise decrease in film thickness³⁶⁻³⁸.

Several recent experimental studies have served to highlight the role of the confining surfaces. Pressure drop-flow rate measurements across cylindrical nanopores using short n-alkanes and OMCTS reported only a modest deviation from bulk fluid behavior³⁹. These findings implied liquid-like mobility of the molecules immediately adjacent to the solid surface. A similar conclusion can be drawn from surface force apparatus measurements of normal forces between organically coated surfaces intermediated by a thin polymer melt film⁴⁰. Films of branched short chain molecules exhibited no yield

stress when subjected to shear²⁸ and responded like bulk liquids, albeit with a bulk viscosity a couple of orders magnitude higher than the viscosity of the bulk fluid.

The spectrum of behavior observed in polymeric thin films prompted several simulation studies that resulted in a variety of discoveries. The first simulation studies⁴¹⁻⁴³ were consistent with a liquid-like pattern of interfacial and thin film behavior. Subsequent studies stressed the importance of solid surface topography⁴⁴ and revealed possibility of epitaxial crystallization⁴⁵. Simulations on short chain molecules employing a simple bead-spring model reported a sharp drop in the intra-layer diffusion (glassification)^{6, 46}. Other molecular dynamics simulations of n-octane films confined between structured solid surfaces using more realistic models for the octane chains (bend angle potentials and torsional potentials) reported on the segmental behavior in the first layer⁴⁷⁻⁵¹. Koopman et al.⁴⁹ reported on the formation of highly ordered microdomains inside the layer immediately adjacent to the solid surface. The domains possessed the order of "rotator" hydrocarbon phases, which were stable over the nanosecond time scale and their directionality was imposed by the underlying square solid matrix.

The experimental and simulation findings over the past decade have revealed a rich and diverse behavior of interfacial and confined liquid films. In some cases the behavior could be classified as liquid-like with only moderate deviations from the bulk^{41, 42, 28, 39}. Other experiments and simulations suggested glassy features^{46, 6}. Furthermore, several experiments and simulations observed the development of solid-like features inside the first layer next to a physisorbing surface^{25, 44, 45, 52, 34, 35, 48-50}.

The evidence from experiments and simulations inevitably raises the question: What are the factors that are responsible for the solid-like or liquid-like features observed in thin polymeric films? To answer this question, one has to identify the factors characteristic to a thin film system and assess their relative importance. The factors that influence the structure and properties of the interfacial films can be classified into the following four categories:

- a) thermodynamic conditions of the system (temperature and pressure)
- b) energetics of the solid-segment interaction
- c) topography of the solid surface
- d) architecture of the liquid molecules

Clearly, the behavior of the film is determined by a complex interplay of all the above factors. Any attempts to tailor thin films would require at least a qualitative understanding of the effects and relative importance of each of these factors. The objective of the research currently being conducted is to contribute towards reaching such a level of understanding. Our approach consists in isolating one factor and determining its effect on film properties. The thermodynamic conditions and energetics of solid-segment interactions are easily quantifiable. Furthermore, since solid-like thin film behavior was observed for a variety of liquid molecules whose architecture was not particularly commensurate with the solid-substrate used (cleavage plane of mica), it seems reasonable to conclude that factors a) and b) are more important.

In accordance with our objective we have opted to simulate thin films of n-octane confined between atomically smooth (flat) solid surfaces under conditions of constant

pressure and constant temperature (i.e., fix the thermodynamic conditions). The choice of n-octane offers several advantages, since extensive data from previous simulation studies was available^{53, 54, 55, 56, 57, 49}. Also, several experiments investigated thin films of linear alkanes^{58, 24, 25, 52}. The geometrically flat surface eliminates the role of surface topography and allows us to focus on the role of energetics and pressure.

In chapter 4 results of Molecular Dynamics simulations on ultra thin films of n-octane chains are reported. These simulations study the role of the surface segment energetics, normal pressure and isotropic pressure.

2.2 Studies of Solid-Polymer Solution Interfaces

The earliest theories dealt with a solid surface-single polymer chain interface⁵⁹⁻⁶⁵. Since then, there have been considerable advances in the study of polymer adsorption. Roe⁶⁶ gave the first comprehensive treatment of adsorbed polymer chains. Helfand⁶⁷⁻⁶⁹ improved this theory by removing the assumption that each segment contributes equally to segment density at any given distance from the interface. These theories had the short coming of not correctly accounting for end effects (polymer chain tails). Scheutjens and Fleer (SF theory) put forward a generalized model, which could be solved numerically, for the adsorption of interacting chains by weighing all the steps with the appropriate Boltzmann factor^{18, 19}. De Gennes used scaling arguments together with the concept of self similarity and derived expressions for the overall segment density profile⁷⁰. Very recently, Semenov and coworkers have treated the solid-polymer solution interface at a wide range of bulk concentrations using self consistent mean field theory and scaling arguments⁷¹⁻⁷³. The mean field theoretical approaches have analyzed the conformational

characteristics of the adsorbed chains in terms of their trains, tails and loops. These theories are briefly discussed later in this chapter.

Several experimental techniques are currently used to probe the solid-polymer interfaces. Indirect methods remove the bulk polymer solution after adsorption, to evaluate the adsorbed amount of polymer while the direct methods probe the interface without removing the bulk polymer solution. In a system where the bulk polymer solution is dilute and the surface layer quite thick evanescent wave methods, neutron reflectometry⁷⁴, optical reflectometry⁷⁵ ellipsometry⁷⁶, surface plasmon resonance⁷⁷, surface-enhanced Raman scattering⁷⁸ and the quartz crystal microbalance⁷⁹ may be used on single flat surfaces without removing the bulk polymer solution. These methods can give a direct estimate of the adsorbed amount and adsorbed layer thickness. Small angle neutron scattering⁸⁰ can be used to probe the density profiles of adsorbed polymer layers. Another method that measures the adsorbed polymer layer thickness is Atomic Force Microscopy⁸¹.

The effect of adsorbed polymer on concentrated colloidal suspension stability has been studied using atomic force microscopy⁸²⁻⁸³. The topography of polymer film-air interface and film thickness can also be determined with the help of Atomic Force Microscopy⁸⁴.

The available experimental methods cannot give direct information on the polymer chain conformational characteristics. Computer simulations provide a very valuable tool to investigate the macromolecules, their conformations and their dependence on physical conditions. The literature on computer simulation of macromolecules is vast¹⁰. The

literature on other types of systems such as end grafted chains, copolymers, polyelectrolytes and chemisorbed systems is large. The conformational properties of end grafted chains have been studied in detail by several authors⁸⁵⁻⁸⁷. Polyelectrolyte molecules in dilute bulk solutions have been simulated and found to undergo a cascade of transitions with changing pH⁸⁸. Below we discuss the literature directly pertinent to adsorbed neutral polymer chains.

Physisorbed homopolymers are difficult to study since they involve very long structural relaxation times⁸⁹ and hysteresis effects⁹⁰. Many of the studies are for a single chain interacting with an adsorbing surface^{91, 92}. The polymer chain conformational features at a solid-polymer melt interface have been studied by Bitsanis and ten Brinke. Recently, there have been numerical results reported for the statics and dynamics of adsorption from semi-dilute solutions⁹³⁻⁹⁶. Adsorbed polymer layers in equilibrium with a semi-dilute solution were found to exhibit a concentration profile that decays as $z^{4/3}$ close to the surface as predicted theoretically by de Gennes³². The earlier studies have so far investigated the semi-dilute and the concentrated regimes.

The theoretical treatment of polymers at interface has addressed the long chain limit of structural characteristics of polymer chains, while the simulation studies could only be conducted on relatively short chains. For this reason, testing the theory with molecular simulations has been a difficult task. However, since relatively short chains can still form distinct proximal and distal regimes, it should be possible to test the validity of the scaling and mean field theories in these two regimes. In this work we endeavor to

examine the solid-dilute polymer solution interface theory under theta solvent conditions. This interface under athermal solvent conditions has been studied recently in our group.

2.2.1 Scaling Theory

De Gennes³² constructed the scaling form of the bulk correlation length ξ in an athermal solvent to be $\phi^{-1/4}$. Using the same argument, ξ in general scales with the concentration as $\phi^{-1/m}$ where $m = 3-1/\nu$, $\nu = 0.5$ for ideal chains and $\nu = 3/5$ for chains with excluded volume effects. This relationship is based on the requirement that the mesh size is comparable to the coil size in semi-dilute solutions and gets smaller with increasing concentration. The segment density profile close to an attractive solid surface and a semi-dilute polymer solution is predicted to decay as z^{-m} since the bulk correlation length ξ scales with the distance z from the surface. Hence the segment density profile for semi-dilute polymer solution in contact with an attractive surface decays as z^{-1} for theta solvents and as $z^{-5/3}$ for good solvents. This exponent of decay increases as one goes from semi-dilute to concentrated bulk conditions⁹³.

2.2.2 SF Theory

Scheutjens and Fleer^{18, 19} have used a lattice model to describe the polymer chains. The interactions between polymer chain segments are included through the Flory χ parameter. Using the Boltzmann weight of growth near the solid surface and in bulk along with the Bragg-William (random mixing) approximation, the distribution function of polymer chain conformations is formulated. By differentiating the partition function with respect to the number of chains having a particular conformation an expression is derived that gives the numbers of chains in each conformation at equilibrium.

Calculations are carried out numerically for chains at different bulk concentrations. The segment densities due to segments belonging to trains, tails, loops and free chains are obtained. Setting the Flory χ parameter to 0.0, gives athermal solvent conditions and setting it to 0.5 gives theta solvent conditions.

In their original papers, Scheutjens and Fleer study chains up to 1000 segments long under theta and athermal solvent conditions. The SF theory is a more accurate theory than the earlier theories due to Roe and Helfand, since the end effects are properly accounted for in the SF theory.

2.2.3 Two Order Parameter Mean Field Theory of Semenov and coworkers

Using Self Consistent mean field calculations^{71, 72}, Semenov and coworkers have predicted the conformational features of polymer chains that adsorb from a theta solvent on to a physisorbing solid surface. Using the ground state dominance approximation, the concentration profile is derived to be

$$\varphi(z) = \varphi_0 \coth^2 \left(\frac{z}{2\xi} + \beta \right) \quad (2.1)$$

where z is the distance from the solid surface, $\varphi(z)$ is the concentration, $\xi = a/\sqrt{2\varphi_0}$ is the bulk correlation length and $\beta = 1/2 \arcsin h(b/\xi)$. The parameter b contains the information of the solid surface-polymer segment interaction energy. In the formal limit $\varphi_0 \rightarrow 0$ corresponding to an equilibrium with an extremely dilute bulk solution

$$\varphi(z) = \frac{2}{(z+b)^2} \quad (2.2)$$

This result is valid for long chains at distances less than the coil size R , i.e., in the regime where the loops are dominant. Under these conditions, the scaling relationships of loop concentration (φ_l) and tail concentration (φ_t) profiles are given as follows.

$$\varphi_l \sim \frac{1}{z^2} \quad \varphi_t \sim \frac{z}{Nb} \quad b < z < z^* \quad (2.3a)$$

$$\varphi_l \sim \frac{(Nb)^3}{z^8} \quad \varphi_t \sim \frac{1}{z^2} \quad z^* < b \ll R \quad (2.3b)$$

Here z^* is the point where the loop and tail concentration profiles cross each other.

The authors derive limiting functional forms of the loop and tail concentration profiles using a two order parameter formalism for the extremely dilute solution limit, the dilute regime, the semidilute regime and the concentrated regime of the bulk solution. The interfacial region is divided into several regions depending on the bulk concentration. In the dilute case three distinct regions can be distinguished a) Proximal region closest to the wall within a distance d ($z \ll z^*$), comparable to the monomer size in the limit of strong adsorption b) the central region in the intermediate range ($d < z < \lambda = \epsilon^{-1/2}$), where

$$\epsilon = \frac{1}{N} \log \frac{N^2 B^2}{4\varphi_0}, \quad B \sim 1 \quad (2.4)$$

and c) the distal region ($z > \lambda$).

The concentration profiles for the extremely dilute case ($\varphi_0 \ll 1/N$) and the dilute case are:

$$\varphi_l = \frac{2}{z^2} \quad \varphi_t = \frac{4z}{(z^*)^3} \ln\left(\frac{z^*}{z}\right) \quad b \ll z \ll z^*$$

$$\begin{aligned}\varphi_i &= \frac{1800(z^*)^6}{z^8} & \varphi_i &= \frac{20}{z^2} & z^* << z << \lambda \\ \varphi_i &\sim \frac{(z^*)^6}{\lambda^8} e^{-2z/\lambda} & \varphi_i &\sim \frac{1}{\lambda^2} e^{-z/\lambda} & \lambda << z << D\end{aligned}\quad (2.5)$$

The predictions for dilute and the extremely dilute case have slightly different profiles for φ_i , the concentration due to free chains.

The two order parameter theory has been compared with the numerical results of Scheutjens and Fleer¹⁹. The two theories are in good agreement for calculations made for very long chains ($N=100,000$).

In chapter 5 we examine the theoretical predictions of Semenov and coworkers and the scaling laws of de Gennes, by simulating a physisorbing solid surface in contact with a dilute neutral polymer solution under theta conditions.

CHAPTER 3

COMPUTER SIMULATION AND MODELING

Computer simulation provides a direct route from the microscopic details of a system to macroscopic properties of experimental interest (equation of state, structural order parameters, transport coefficients, etc.). Furthermore, it may be impossible to carry out experiments under extreme conditions, while a computer simulation of the material would be perfectly feasible. An important advantage of computer "experiments" is that they allow precise control on the various relevant factors, and make it possible to study the influence of any single factor.

Simulation and modeling of polymeric interfaces requires careful attention. Choosing appropriate models for simulation is a balance between the computational cost and the degree of accuracy. While a detailed atomistic level modeling may be necessary to study segmental scale phenomena, a coarse lattice or bead spring model might suffice for investigating large scale features.

The two most common simulation techniques employed in simulating liquids are Molecular Dynamics and Monte Carlo method. Molecular Dynamics follows the dynamics of a classical system by integrating the equations of motion. Monte Carlo simulations explore the configurational space by allowing random unphysical moves. While Molecular Dynamics simulations can provide reliable information on the dynamic

properties of the system (diffusivity, viscosity etc.), Monte Carlo simulations are often better suited to explore the configurational space more efficiently.

3.1 Brief History

Molecular simulations had their beginning in the 1950s. The principal methods used in molecular simulations of matter are Monte Carlo and molecular dynamics methods. The early work of Metropolis et al. in 1953 laid the foundation of modern Monte Carlo simulations⁹⁷ (the term was inspired by the role random numbers play in the method). Monte Carlo techniques sample the configurational space to generate a set of configurations of the system that is representative of an equilibrium ensemble of the true system.

Molecular dynamics is concerned with the time evolution, under the laws of classical mechanics, of systems of particles, interacting via conservative forces. The trajectories of the particles in the system are calculated and this method is most suitable for studying dynamic properties such as transport coefficients. However, it is computationally more intensive than Monte Carlo methods.

Early molecular dynamics simulations of systems of hard spheres were initiated by Alder and Wainwright⁹⁸⁻¹⁰⁰. It was later that a successful attempt was made to work with the equations of motion for a set of Lennard-Jones particles¹⁰¹. Subsequently the field of molecular dynamics simulations developed rapidly, and was extended from atomic systems to more complicated systems, like water, clays, polymers, colloids, biomolecules etc.^{37, 53, 102, 103}. These efforts improved our understanding of complex phenomena like phase transitions and behavior at interfaces¹⁰⁴⁻¹⁰⁶.

Molecular simulations of fluids and polymers are now very widely used and several books and reviews elaborating these techniques are available^{10, 107-109}.

3.2 Tricks of the Trade

Two important "tricks" employed in performing both Molecular Dynamics and Monte Carlo simulations make them feasible. A real system considered will have an enormous number of particles ($>10^{20}$) and it is impossible to calculate the interactions among all these particles even with the fastest of super computers. So computer simulations are performed on a small number of molecules, $100 < N < 10,000$. Such a small system would have a very high surface area to volume ratio and the molecules on the surface will experience quite different forces from the bulk. The problem of surface effects is largely overcome by considering periodic boundary conditions.

3.2.1 Periodic Boundaries

Figure 3.1 contains a two-dimensional schematic illustration of the periodic boundaries. As shown in the figure, a periodic cell (highlighted with thick boundary line) is reproduced infinitely in all the directions. When a particle, say A, moves out of one of the boundaries, all its periodic images undergo the same move. Consequently, another particle enters the main cell from the opposite boundary as illustrated.

3.2.2 Nearest Neighbor Lists

Another technique used to reduce the time taken for a molecular simulation is achieved by using neighbor lists. There are several very efficient data structure schemes available now such as KD trees, linked cells¹¹⁰ and Verlet lists¹¹¹. A comparison of these methods was made by Liu¹¹². We use the Verlet list in our molecular dynamics studies.

The longest range forces in a non-polar system of particles go as r^{-6} and the forces between particles that are more than a few segmental diameters apart can be neglected. Beyond a distance of 2.2σ (σ is the particle diameter), the forces between particles were found to have negligible impact on the system properties¹¹³. By maintaining a list of nearest neighbors for each of the particles, and using this list for computing intermolecular interactions, the computational expense can be reduced substantially without sacrificing accuracy. In the schematic of figure 3.1, the neighbors B and D exert a significant potential on C, where as the particles A and E are too far.

3.3 Initial Configurations

3.3.1 Molecular Dynamics Studies

In Molecular Dynamics simulations, the knowledge of an initial configuration (spatial coordinates) and velocities of the particles in the system is essential to compute the time evolution of the particle trajectories. This is especially significant for chain molecules. Several methods have been used to generate initial configurations^{114, 109}. For our problem the Monte Carlo method proposed by Gupta et al.⁵⁶ has the distinct advantage of generating a random configuration with simultaneous equilibration procedures. Consequently, this method is capable of generating realistic configurations and has been used to develop starting configurations for our simulations. In a system of particles at thermal equilibrium, the velocity distribution of the particles is Gaussian. Generating such a set of initial velocities is a computationally simple task.

3.3.2 Monte Carlo Studies

In lattice Monte Carlo simulations the generation of initial configurations involves random growth of chains starting from arbitrary points on a lattice. However, such a method may not successfully grow the chains to their full length. To generate good initial configurations we use the method proposed by Kolinski et al¹¹⁴. This method of simultaneous growth and equilibration was successfully adopted by Bitsanis and ten Brinke⁷ to simulate confined polymer melts.

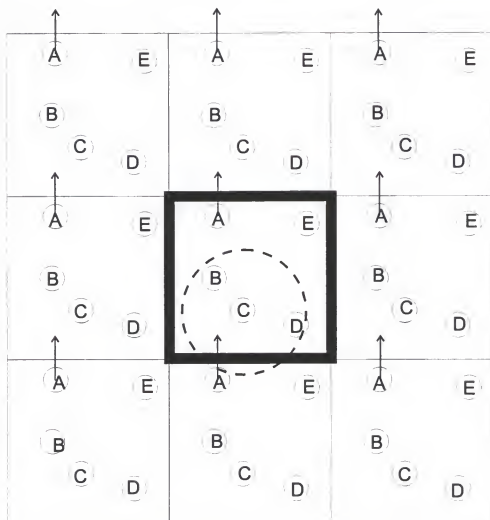


Figure 3.1. A 2-dimensional illustration of periodic boundary conditions. As particle A crosses a boundary, its periodic image enters from the opposite boundary. The nearest neighbors of particle C, that make a significant contribution to the forces on C lie in the dotted circle.

CHAPTER 4

SIMULATIONS OF ULTRA THIN FILMS OF N-OCTANE

4.1 Introduction

In Chapter 2, it was seen that there has been indirect evidence of the solidification of thin layers of oligomers confined between physisorbing surfaces. However, there has been no clear study of the role of surface energy and thermodynamic conditions (T and P) on the structural features of oligomer films.

In this chapter we present results of Molecular Dynamics simulations of thin films of n-octane confined between geometrically flat surfaces. In section 4.2 the modeling and simulation aspects of the systems of interest are discussed. Section 4.3 describes the methods for analyzing the statistical data generated by the simulations. The three systems of interest that were simulated are described in section 4.4. In the subsequent section 4.5, results of the first two sets of simulations were discussed. Finally, some simulation attempts made to study ultra thin films of n-octane under isothermal, isobaric conditions and the reasons for their limited success are presented in section 4.6.

4.2 Molecular Model and Simulation Method

4.2.1 Introduction

The simplest monomeric unit in linear organic molecules is methylene ($-\text{CH}_2-$). Furthermore, polyethylene ($\text{CH}_3-(\text{CH}_2-\text{CH}_2)_n\text{CH}_3$) is the simplest and one of the most

commonly used polymers. Consequently, alkanes and polyethylene were very well studied and there exist reliable data on these compounds^{2, 115}.

n-Octane was a natural choice for simulations since its length is approximately equal to the typical size of a train in dense proximal interfaces. Actually C_8 is somewhat shorter than the typical train size (which would be about C_{11} - C_{12}). However, there is a lot of simulation data on bulk C_8 that render it a very good candidate for our study.

An n-octane molecule (C_8H_{18}) has several hydrogen atoms that are significantly smaller and lighter than the carbon atoms. It is computationally wise to approximate the methyl (CH_3) and methylene (CH_2) units as identical, spherical units with their centers of mass at the carbon atom center. This model is referred to as the "United Atom" model. Another model, "Anisotropic United Atom" model, places the center of mass of the segment slightly away from the carbon atom center, to compensate for the effect of the hydrogen atoms. The anisotropic united atom model has been shown to reproduce the real behavior of systems accurately^{116, 117}. Our choice of the United Atom model is commensurate with our objective to gain insight into the structural patterns at solid polymer melt interfaces and to predict semi-quantitatively the conditions under which these transitions take place. Also, it offers a significant advantage in terms of computational time¹⁰⁰.

A schematic of the backbone of an n-octane chain (United Atom model) is shown in figure 4.1a. The segments are linked to one another by Carbon-Carbon chemical bonds that are the source of bond-length potential. The tetrahedral structure of chemical bonds introduces an angle between any three successive segments (bond-angle potential).

Furthermore, in a sequence of four segments (figure 4.1b), depending on the position of the fourth segment, the potential energy of the configuration changes (torsional or dihedral potential). A trans angle has the lowest energy and gauche angles represent the other two local minima of the potential.

Earlier simulation models used by Ryckaert and Bellemans⁵³ (1978) used a semi-rigid model in which the bond length and the bond angle were constrained. The algorithms used were also such that this constancy of bond lengths and bend angles was not violated. But the bond stretch and bend are believed to be important degrees of freedom to be included in realistic simulations of alkane molecules^{54, 55}. Also, torsional relaxation is shown to be a key mechanism in alkane diffusion next to solid surfaces^{56, 118}. It is also known that the two types of systems, one having rigid constraints, and the other with flexible constraints differ in equilibrium properties¹¹⁹. Finally, the algorithms for constrained molecular dynamics are considerably more complicated and their computational advantage only marginal. Therefore, we opted for a fully flexible model, where both the bond lengths and bend angles are allowed to fluctuate around their mean values.

4.2.2 Molecular Interactions

All the intramolecular interactions described above are modeled in our simulations as follows. Individual chain segments are modeled as point particles connected by spring-like valance bonds subject to a harmonic potential energy :

$$U_{b,j} = \frac{1}{2} k_b (b_j - b_0)^2 \quad (4.1)$$

where b_0 is the equilibrium bond length and k_b is the spring constant. The valence angle θ between successive pairs of bonds is maintained close to the tetrahedral value θ_0 by a potential quadratic in $\cos\theta$.

$$U_{\theta,j} = \frac{1}{2} k_{\theta} (\cos\theta_j - \cos\theta_0)^2 \quad (4.2)$$

Further, the torsional angle (ϕ) is constrained to lie mainly in trans and gauche rotational states by the following potential as used by Ryckaert and Belleman⁵³:

$$U_{\phi,j} = k_{\phi} \sum_{n=0}^5 a_n \cos^n \phi_j \quad (4.3)$$

The values of the constants in the above potentials are listed in Table 4.1.

The interactions between segments belonging to different chains and segments separated by more than three segments are given by the truncated Lennard-Jones potential.

$$U_L = \begin{cases} 4\epsilon \left[\left(\frac{\sigma}{r} \right)^{12} - \left(\frac{\sigma}{r} \right)^6 \right] & r \leq 2.2\sigma \\ 0 & r > 2.2\sigma \end{cases} \quad (4.4)$$

The parameters ϵ and σ are obtained by fitting experimental data to the above equation and represent the negative well depth and the segment diameter respectively. The potential has a long range attractive tail (r^{-6}), and a steep repulsive wall at distances less than $r \sim \sigma$.

It is convenient to perform calculations in reduced molecular dynamics units, where the values of ϵ , σ and the mass of the methylene segments are set to unity. Table 4.1 lists various quantities in SI and Molecular Dynamics units.

Table 4.1. Parameters of inter and intra-molecular potentials

Quantity	In MD units		In SI units	
Intermolecular potential				
ϵ	1.0		500 J/mol	60.1K
σ	1.0		3.9×10^{-10} m	
m	1.0		14.25 g/mol	
Intramolecular potential				
k_b	10 000	(ϵ/m^2)	3.46×10^{25} (J/m ² /mol)	
k_θ	1000	(ϵ)	50 000 (J/mol)	
k_ϕ	16.4	(ϵ)	820 (J/mol)	
b_0	0.39	(σ)	1.48×10^{-10} (m)	
θ_0			109.47 ^o	
$\Delta E(t \leftrightarrow g)$	5.78	(ϵ)	2892 (J/mol)	
Kinetic barriers				
$\Delta E^{\text{act}}(t \leftrightarrow g)$	24.36	(ϵ)	12 178 (J/mol)	
$\Delta E^{\text{act}}(g^+ \leftrightarrow g^-)$	88.37	(ϵ)	44 184 (J/mol)	
Coefficients of torsional potential	$a_0=1.116$ $a_4=3.156$	$a_1=1.462$ $a_5=-3.788$	$a_2=-1.578$	$a_3=-0.368$

The interactions between the polymer segments and the smooth solid surface were governed by the 10-4 Lennard-Jones potential.

$$U_s = 2\pi\epsilon_s\rho_s \left[0.4 \left(\frac{\sigma_s}{z} \right)^{10} - \left(\frac{\sigma_s}{z} \right)^4 \right] \quad (4.5)$$

In the above equation z is the surface-segment distance, ρ_s the number density of a solid layer and ϵ_s is the Lennard Jones energy parameter for the interaction between segments and a (fictitious) surface "atom". σ_s is the arithmetic average of the length parameters of the segments and surface atoms. This potential is obtained by integrating the discrete interactions between the surface atoms and segments over an entire layer¹²⁰. After the

integration, the resulting surface becomes perfectly smooth and will lack any topographical features. Clearly, for such a surface only the product $\epsilon_{sl}\rho_s$, not the individual factors, is meaningful. Therefore, ρ_s is arbitrarily assigned the value 1.0 in molecular dynamics units. Furthermore, σ_{sl} , which determines the size of the now smeared solid atoms has a trivial effect in the case of smooth surfaces. σ_{sl} was assigned the value of 1.0 in molecular dynamics units.

The factors that influence the properties of interfacial films can be classified as a) thermodynamic (temperature and pressure) b) solid-segment energetics (ϵ_{sl}) c) solid surface topography and d) liquid molecule architecture. The solid surface architecture is very material specific. In order to understand the role of solid segment energetics, we eliminate the influence of surface topography by considering the 10-4 Lennard-Jones potential. The 10-4 Lennard-Jones potential represents the interaction potential between a particle and an infinite, geometrically smooth surface.

4.3 Data Acquisition and Data Analysis in Molecular Dynamics

In the simulations we perform, the classical equations of motion for segments are integrated numerically using Verlet's algorithm. The net force acting on a segment at a given instant is computed using the appropriate intramolecular and intermolecular potentials. By integrating the equations of motion for the individual segments, the trajectories of the segments are computed:

$$m_j \frac{d^2 \mathbf{r}_j}{dt^2} = \mathbf{F}_j = -\nabla_{\mathbf{r}_j} U \quad (4.6)$$

In the above equation \mathbf{r}_j denotes the position vector of the center of mass of the segment j of mass m_j , \mathbf{F}_j denotes the force on segment j , and U is the total potential energy (sum of

intra and inter-molecular potentials). A number of procedures have been used historically to integrate such second order differential equations¹⁰⁷. We employ Verlet's central difference prediction algorithm:

$$\mathbf{r}(t+h) = 2\mathbf{r}(t) - \mathbf{r}(t-h) + h^2 \mathbf{a}(t) \quad (4.7)$$

The error in the predicted coordinates is of the order of h^4 . The estimated velocity is

$$\mathbf{v}(t) = \frac{\mathbf{r}(t+h) - \mathbf{r}(t-h)}{2h} \quad (4.8)$$

The time step h is typically chosen an order of magnitude smaller than mean collision time, which for Argon corresponds to $\sim 10^{-13}$ sec¹⁰¹.

From the trajectories generated in the phase space, the static properties are evaluated as time averages

$$\langle A \rangle = \frac{1}{N} \sum_{i=1}^N A(\tau_i) \quad \text{where} \quad \tau_i = \frac{h(i-1)}{N} \quad (4.9)$$

Here, for example, A could be kinetic energy, pressure, density, etc.

The transport properties are calculated using the time correlation function formalism. The linear response theory¹²¹, expresses the transport coefficients as the time integrals of the appropriate time correlation functions. The relevant time correlation functions can be written as an ensemble average or as a time average along the phase space trajectory. These two are equivalent according to the ergodic hypothesis. The time correlation function of two dynamical variables A and B can be expressed as

$$\langle A(t)B(0) \rangle = \lim_{T \rightarrow \infty} \frac{1}{T} \int_0^T d\tau A(t+\tau)B(\tau) \quad (4.10)$$

The average denoted by the $\langle \dots \rangle$ is an ensemble average over an equilibrium distribution.

4.4 System Description

We simulated several systems to study the effect of pressure and solid-methylene unit energetic affinity in inducing structural transitions at the solid-polymer melt interface. All systems had periodic boundary conditions imposed in the x and y directions. The periodic cell had a side of 9.0σ (about 3.54 nm). An n-octane molecule in its all trans configuration measures $\sim 2.2\sigma$. The size of the box was large enough to preclude chain connectivity artifacts produced because of the periodic boundary conditions. In all the simulations the octane films were confined between geometrically smooth solid boundaries in the z direction. The thickness of the film was determined by the following two requirements: a) the development of three methylene segment layers parallel to the surfaces and b) the attainment of the desired value of pressure normal to the solid surfaces. Furthermore, the temperature was kept very close to its prespecified value by velocity scaling every 50 time steps, after equilibration. Therefore, our simulations were performed in a constant N,V,T ensemble (canonical). However, the fixed film thickness resulted in a selected value of average “normal” pressure. This implies that our films were in thermodynamic equilibrium with a bulk reservoir at the same temperature as the film and bulk pressure equal to the normal component of the pressure tensor inside the film. Hence the film and the bulk reservoir had the same chemical potential.

4.4.1 Effect of Solid-Segment Affinity

The effect of solid segment affinity was studied at constant normal pressure as described above. We performed simulations at the following conditions to determine the role of surface-segment energy:

- a) temperature 300.5K and (normal) pressure close to 0 bar for the following values of the solid-segment energy parameter ϵ_{sl} : 180.3K, 240.4K, 300.5K, 360.6K, 420.7K and 480.8K.
- b) temperature 360.6K and (normal) pressure close to 700 bar for the following values of the solid-segment energy parameter ϵ_{sl} : 360.6K, 540.9K, 601K, 661.1K, and 721.2K.

Our systems of interest were anisotropic and have strong confinement effects. The simulations were in a canonical ensemble where the N , V and T were kept constant. The average normal pressure is kept close to a desired value by adjusting V to an appropriate value in each of the simulations. Each of these simulations represented an average normal pressure. Simulating an isothermal-isobaric ensemble where the components of the pressure tensor were kept constant and the volume was allowed to fluctuate around an average value was a natural extension of the work. Hence we attempted to simulate an isothermal-isobaric ensemble at constant N , P and T by allowing the changes in the shape and size of the periodic box and the slit width. The study of this system presented several problems and the results obtained were not always trustworthy. We discuss the results of these simulations in greater detail in section 4.6.

4.4.2 Effect of Normal Pressure

The effect of normal pressure was studied by fixing the solid-segment affinity at a constant value. The distance between the solid walls was adjusted to yield different specific volumes resulting in a range of pressures. Each simulation was performed in a canonical ensemble at a constant average normal pressure.

We performed simulations at the following conditions to determine the role of pressure:

- c) temperature 360.6K and solid-segment energy parameter (ϵ_{sl}) 601K for the following values of normal film pressure : -40 bar, 150 bar, 490 bar, 980 bar, 1320 bar, 710 bar, 1090 bar.

Bulk octane is a liquid under all these thermodynamic conditions. The melting point and boiling point of n-octane are 216.4K and 398.8K at room conditions (1 bar pressure). Estimates using the Clapeyron equation showed that increasing the pressure on bulk n-octane to 1500 bar elevates its melting point by only 10 to 20 K.

4.5 Results and Discussion

In this section, we discuss the effect of increasing solid-segment affinity (ϵ_{sl}) and increasing normal pressure in inducing structural transitions in thin n-alkane films. Since both normal pressure and ϵ_{sl} induce qualitatively similar behavior in the film we present the results of all the simulations simultaneously.

4.5.1 Simulation Results

Liquid to solid transitions in bulk materials usually result in a modest increase of the density upon solidification. Figure 4.2 shows the average segment density of the simulated n-octane films as a function of ϵ_{sl} for the two temperatures studied. The overall shape of the curves in figure 4.2 is similar to typical high affinity adsorption isotherms. A relatively abrupt densification occurs between the ϵ_{sl} values of 300.5K and 360.6K in the low temperature curve. This feature seems to be too weak to be observed in the high

temperature data. Nevertheless, the foregoing discussion will show that there are convincing arguments in favor of its existence.

Figure 4.3 contains the segment density profiles normal to the solid surfaces. The distance axis is symmetric about the mid-plane of the films. The requirement of constant normal pressure (figures 4.3a and 4.3b) results in a gradual decrease of film thickness with increasing solid-methylene unit affinity. Similarly, the increasing pressure at constant ϵ_{sl} results in decreasing film thickness (figure 4.3c). In all systems studied the film consisted of three sharply defined segment layers. The layers show gradual densification with increasing ϵ_{sl} (figures 4.3a and 4.3b) and pressure (figure 4.3c).

Figure 4.4 shows the normal component of the pressure tensor as a function of the specific volume of the film. The shape of the curve in figure 4.4 is typical of PV isotherms involving phase transitions. Metastable states can be observed as a result of the finite duration (3–4 nsec) and finite system size in the simulations. This is a well-known phenomenon in canonical ensemble simulations of finite system size^{100, 122, 107}. The specific volume of the film is much lower (or the density much higher) than that of bulk n-octane (1.4235 cc/gm at 298K and 1bar) which is to be expected since it is next to a highly adsorbing surface.

The in-layer pair correlation function (PCF) measures the degree of structure in each layer. It is defined as the (normalized) probability of finding two segments separated by a given distance. It is conventional to set the probability of finding two segments infinitely apart to unity. The in-layer pair correlation function $g(r)$ is the sum of the contributions of i) intramolecular PCF, $g_{intra}(r)$ (i.e., PCF of segments belonging to the same chain) and

ii) intermolecular PCF, $g_{\text{inter}}(r)$ (i.e., segments belonging to different chains). The general shape of the in-layer PCF curves for octane chains is illustrated in figure 4.5. At distances less than $\sim 2\sigma$, the intramolecular pair correlation function has several peaks that correspond to first and second neighbors, and 1-5 torsional angles. In the systems under observation, the large peaks that correspond to first and second neighbors along the chain as well as the features related to 1-3 trans angles, have much higher intensity than those associated with the intermolecular pair correlation function. These peaks would obscure the scale of the drawing and have been omitted in the later figures, to elucidate the features of the intermolecular structural order.

Figures 4.6 and 4.7 contain the in-layer pair correlation function for the first and the middle layers respectively. One immediately apparent feature is that, all the curves belong to either one of the two distinct groups. In figures 4.6a and 4.7a, corresponding to the low temperature (300.5K) system, the shape of the pair correlation function undergoes an abrupt change between the ϵ_{sl} values of 300.5K and 360.6K. A similar change (figures 4.6b and 4.7b) is evident between the ϵ_{sl} values of 601K and 661.1K for the system simulated at 360.6K. Upon changing the pressure from 1320 bar to 710 bar, a similar abrupt transition of the in-layer pair correlation function is observed (figures 4.6c and 4.7c).

Such abrupt changes in the shape of the pair correlation curves are "signatures" of first order phase transitions. The middle layer pair correlation function curves (figure 4.7) show a more distinct transition relative to the first layer curves (figure 4.6). This is to be expected since the effect of the solid surface diminishes as the solid-segment

distance increases. Consequently, the middle layer is less ordered than the first layers below the transitions. The sudden transition in the first layer segments induces an order in the middle layer segments that results in the precipitous change of the shape of the middle layer PCF curves.

Another important feature in figures 4.6 and 4.7 is the development of well-defined second and third peaks. Such peaks indicate long range intermolecular order within the layer and suggest regular packing of octane chains. Such long range order is possible only if the molecules adopted extended, rod-like configurations.

The percentage of trans angles in the film quantifies the configuration of the molecules. The abrupt change in the shape of the pair correlation functions at the critical ϵ_{sl} and pressure values is accompanied by a precipitous increase in the fraction of trans torsional angles. Figure 4.8a plots the percentage of trans angles as a function of the solid-segment affinity ϵ_{sl} . The change is more pronounced at the low temperature where the fraction of trans angles jumps from 0.83 to 0.90 between $\epsilon_{sl} = 300.5\text{K}$ and 360.6K . A milder, yet distinct jump is seen in the high temperature data, between $\epsilon_{sl} = 601\text{K}$ and 661.1K . A similar sharp increase in the fraction of trans angles occurs as the pressure crosses its critical value between 1320 bar and 710 bar (figure 4.8b). The shape of the curve in figure 4.8b is a consequence of the shape of the PV isotherm (figure 4.4). Above the transition, approximately 90% of the torsional angles are trans angles. This implies that about 50% of the chains are in fully extended, rod-like configurations, while the rest ended up with a gauche sequence.

The discontinuous structural changes observed in the film are accompanied by the freezing of molecular migration and rotation, on the time scale of the simulations. The effect of solid-segment energetics and pressure on molecular mobility is best studied by monitoring the mean square displacement and the time correlation functions of the molecular end to end vector. The slope of the former is proportional to the translational diffusion coefficient and the latter to the rotational diffusivity.

Figure 4.9 shows the segmental mean square displacement curves for the three cases studied (effect of ϵ_{sl} at 300.5K, 360.6K and effect of pressure). The time interval covered in these plots is about 0.2 nsec, i.e., 10-20 times shorter than the duration of most simulation runs. Two important observations can be made in these figures. The mean square displacements undergo a sudden drop above the critical solid-segment affinities (figures 4.9a and 4.9b) and the critical pressure (figure 4.9c). The magnitude of the displacement is smaller than the molecular size, implying that the molecules froze in their positions. Direct visualizations of the molecular dynamics simulations confirm this conclusion. Similarly, any significant molecular rotation ceases at the same transition values of ϵ_{sl} and pressure (figure 4.10). The final slope of the mean square displacement and rotational correlation function curves above the critical ϵ_{sl} and pressure values are too low to be determined by the simulations on the nanosecond time scale. The only quantitative statement we can make here is that both translational and rotational diffusivities dropped by at least a factor of 15 as we cross the transition ϵ_{sl} 's and pressure.

4.5.2 Discussion

So far, some of the findings of our simulations were presented. Here, discuss further findings and examine their implications.

Figure 4.11 consists of snapshots of the first layer configurations at four different ϵ_{sl} values: $\epsilon_{sl}=180.3\text{K}$, 300.5K , 360.6K and 480.8K at the temperature of 300.5K . The ϵ_{sl} values include the two immediately below and immediately above the transition threshold. Figure 4.12 contains similar first layer snapshots at the following pressure values: $P = -40, 1320, 710, 1090$ bar. Snapshots of the middle layer of all simulations exhibit similar features. The snapshots of systems simulated at the high temperature contain the same features.

Several interesting characteristics can be observed in these snapshots. One conspicuous characteristic (figures 4.11d and 4.12d) is the presence of two distinct domains with their directors roughly perpendicular to each other. The domains observed above the transition ϵ_{sl} and pressure values were stable over the time scale of our simulations (2-4 nsec). The presence of ordered domains, instead of a uniform ordered phase, lead to the formation of two "grains" throughout the whole film. Each grain typically contained about 20-50 octane molecules. Earlier simulations conducted on smaller systems, with a periodic dimension of 6σ always led to the formation of a uniform ordered phase above the critical values. Therefore, we can conclude that the linear dimensions of the domains should be intermediate between 6σ and 9σ (2.4-3.6 nm). This is close to the domain size inferred from Scanning Tunneling Microscopy experiments^{34, 35}. However, it is also possible that the domains observed are frozen

metastabilities that cannot relax on the time scale of the simulation (a few nanoseconds). Resolving this issue by molecular simulations is extremely difficult, if not impossible. Nevertheless, if such a finding could be trusted, its implications on material properties of thin films would be profound.

So far, we have not classified the ordered phases. Since the octane chains adopt rod-like configurations, the ordered phase could in principle be nematic, smectic or crystalline. These terms refer to the possible types of intralayer order, i.e., they are used to describe layers, which are 2-dimensional entities. The domains possess a high degree of orientational order above the transition (figures 4.11c, 4.11d, 4.12c, 4.12d). Furthermore, there exists also considerable translational order, perpendicular to the molecular end-to-end vector. This is also indicated by the well-developed second and third peaks in the in-layer pair correlation function curves (figures 4.6 and 4.7). These two features (orientational and translational order) combined, already constitute a 2-dimensional smectic phase.

These ordered phases fall short of being fully crystalline since, they do not possess order in the direction parallel to the chain end-to-end vector, resulting from the slight roughness present in the molecular shape. Such an ordering cannot be seen in figures 4.11c, 4.11d, 4.12c, 4.12d and analogous features are absent in the pair correlation function (figures 4.6 and 4.7). So these ordered phases are just short of being fully crystalline octane. They are also different from the "rotator" phases of solid alkanes. In actuality they are more ordered than "rotator" phases, as the molecular skeleton is almost parallel to the solid surface, i.e., the rotational invariance with respect to the end-to-end

vector is broken. From all these observations, one can safely characterize the ordered domains as solids, which could still undergo a solid-solid phase transition to a fully crystalline n-octane film.

Furthermore, no "tilting" transition was observed, corresponding to an abrupt reorientation of the chain skeleton, as that reported in simulations with atomically rough surfaces⁴⁹. This underlines the importance of the subtle role surface topography may play in determining the exact nature of the film.

Though above the transition the film could safely be characterized as a solid (or, at worst a granular solid), it is a poorly organized solid (figures 4.11c and 4.12c) as manifested by the presence of a few large defects (i.e., partial chains in the layer) and several small defects (i.e., gauche sequences in ordered chains).

Immediately below the transition the film is a liquid by any reasonable definition of the term. The strongest argument in support of this statement is molecular mobility, which allows entire octane chains to migrate and rotate on the time scale of 20-30 psec (figures 4.9 and 4.10). However, it is a much more "viscous" and considerably more "ordered" liquid than bulk octane. Just below the transition, in figures 4.11b and 4.12b the strong intermolecular correlations and the relatively extended configurations, facilitate the ordering. The clearly distinguishable second intermolecular peak in figures 4.6 and 4.7 offer quantitative support to the prediction that the liquid is highly ordered.

These simulation findings report liquid to solid phase transitions. They establish that this is a first order transition, since it is characterized by abrupt structural and dynamical changes. They also, quantify the transition as a mild one, at least compared to liquid-

solid transitions in bulk, as it transforms highly ordered liquids to poorly organized solids.

Here we have observed phase transitions resulting from the change in a thermodynamic variable (normal pressure) and due to the change in a molecular quantity (solid-segment affinity). These findings illustrate that the macroscopic state of a nanoscopic film cannot be specified by the thermodynamic state alone, as solid-liquid molecular interactions affect, or even dominate the film properties.

4.5.2.1 Role of solid-segment affinity

These findings on the effect of solid-liquid segment affinity in inducing structural transitions have some important implications. They show that thin films of n-octane molecules confined between smooth surfaces exhibit either solid, or liquid behavior depending on the type of confining surface, and that there do not exist smooth surfaces that produce intermediate behavior. Therefore, they show that the various solid substrates fall in one of the two categories; those that solidify the film and those that do not. There is no smooth transition between the two, for the type of molecules studied.

These simulations also establish that the solidification of thin films does not require the aid of surface topography, although it is possible that topography may promote, or suppress solidification. This provides a natural explanation to the numerous experiments that reported solid-like features of thin films despite the large differences in the commensurability of the architecture of liquid molecules and the topography of mica substrate.

Although gradual increase of adhesive energy of smooth surfaces produces sharp (phase) transitions in the molecular structure and mobility of the confined film, one cannot rule out the full suppression of such transitions when solid topography is highly incommensurate with that of the film structure. By the same token, highly commensurate solids will be expected to enhance further the sharpness of energetically driven transitions.

The cleavage plane of mica used in the SFA experiments is a highly adhesive surface. Estimates of its effective ϵ_{sl} range from 360K to 600K⁴⁰, which places it well above the transition threshold for the "room conditions" simulations discussed i.e., the low temperature, low pressure simulations. According to our simulations the ϵ_{sl} transition threshold is 330K at these thermodynamic conditions. This is very likely an overestimate of the actual critical ϵ_{sl} value of thin octane films. Furthermore, these considerations ignore the possibility of a layer of water irreversibly attached on the cleavage plane of mica, which would considerably raise its effective ϵ_{sl} . Such a monolayer of water on metal oxides would suffice to bring the metal surfaces, which in themselves are slightly below the threshold (250K)¹²³, above the critical ϵ_{sl} values for film solidification.

4.5.2.2 Role of pressure

The confinement lead to a pressure-driven solidification at pressures much lower than those required for similar solidification of bulk n-octane at $T=360.6\text{K}$. The effect of pressure in inducing structural transitions, even at such an elevated temperature (360.6K), emphasizes the critical role normal forces play in the research of thin film characteristics using the surface force apparatus.

4.5.3 Summary

In summary, we have simulated thin films of n-octane molecules that are three segmental diameters wide. The simulations were designed to examine the effect of increasing solid-methylene unit energetic affinity and increasing normal pressure, in introducing structural transitions. The effect of solid-methylene unit energetic affinity was studied at two different temperatures (300.5K and 360.6K). In both cases, the increasing solid-segment energetic affinity resulted in the solidification of the first layer molecules, as the affinity crossed a threshold value (300.5K and 601K). The increasing pressure also induced the same structural transition. This transition is signaled by the abrupt change in the shape of the pair correlation function curves and is facilitated by the precipitous extension of the octane molecules. The abrupt change in the shape of the pair correlation curves is accompanied by the freezing of large scale molecular migration and molecular rotation. Furthermore, we have observed that the n-octane chains formed domains with their directors approximately perpendicular to each other.

The characteristics of the solidified layer, showed that it is slightly more ordered than a 2-dimensional smectic phase, with translational order and considerable order perpendicular to the molecular end-to-end vector. However, the phase is short of being fully crystalline and is quite similar to "rotator" hydrocarbon phases.

Immediately below the transition, the film is a liquid, as illustrated by large scale translational and rotational diffusion. The film is a considerably more "viscous" and ordered liquid than the bulk. The examination revealed that the transition is a first order transition from a highly ordered liquid to a poorly organized solid.

The findings of this work have several important implications. They show that the solidification of nanoscopically thin films is a general phenomenon, that can be brought about by thermodynamic conditions and solid-segment energetics. The structural transitions do not need the aid of commensurate surface topography, though they may be promoted or suppressed by the structure of the underlying solid substrate.

These simulations provide a natural, microscopic explanation to the solid-like features observed in nanoscopically thin films. They show that smooth solid surfaces fall under two categories: surfaces that induce solidification of films and surfaces that do not. Furthermore, they show that the cleavage plane of mica, which is the most commonly used confining surface in most surface apparatus experiments is adhesive enough to induce solidification of the film, and can do so without being topographically commensurate with the liquid molecule architecture.

4.6 Simulations at Constant Isotropic Pressure

Since the system of interest consisted of three segmental layers of n-octane confined between flat surfaces, the system has very high confinement effects (and a large surface to volume ratio). Furthermore, a periodic box of 9σ is also on the segmental scale. It is probable that the predetermined size of the periodic box does not allow for some equilibrium conformational states the system. Naturally, we attempted simulation studies of our system of interest while keeping the pressure tensor (pressure components in the directions parallel and normal to the confining walls) constant. Below, the modifications made to the molecular dynamics code, and results of some simulation studies are

presented. These simulations presented a difficult task and the results obtained were not always trustworthy.

4.6.1 Algorithm for Simulating Constant Isotropic Pressure

Typical algorithms for molecular dynamics simulations in the NPT ensemble involve coupling the system with an external pressure bath or an external variable V , the volume of the simulation box¹²⁴. There are constraint methods that make the instantaneous pressure a constant of the motion by modifying the equations of motion^{125, 126}. Other methods allow for isotropic changes in the volume and shape of the simulation box¹²⁷⁻¹³⁰.

Octane molecules are short linear molecules. The periodic box side used in the previous simulations may be incompatible with some spatial conformations and packing. If the isothermal, isobaric ensemble simulation is to allow efficient packing of n-octane chains, changes in the periodic box shape should be allowed. Hence we adopt the changing box shape algorithm. We allow only changes in the periodic box side in the x and y directions and the distance between the solid surfaces in the z direction. The periodic box always remains rectangular.

The modified equations of motions of such a system are obtained by assigning a box “mass” Q and including the kinetic energy of the box in the Lagrangian. The equations of motion are then written as

$$m\mathbf{s} = \mathbf{H}^{-1}\mathbf{f} - m\mathbf{G}^{-1}\mathbf{G}\mathbf{s}$$

$$Q\mathbf{H} = (\pi - 1P)V(\mathbf{H}^{-1})^T$$

where \mathbf{s} is the scaled position coordinates $\mathbf{H}^{-1}\mathbf{r}$, V is the volume of the box, \mathbf{H} is the transformation matrix whose columns are the three vectors representing the sides of the

box, and $\mathbf{G} = \mathbf{H}^T \mathbf{H}$. P is the desired value of pressure and π is the pressure tensor in the system given by

$$\pi_{\alpha\beta} = \frac{1}{V} \left(\sum_i m (\mathbf{H} \mathbf{s}_i)_\alpha (\mathbf{H} \mathbf{s}_i)_\beta + \sum_i \sum_{j \neq i} (\mathbf{H} \mathbf{s}_{ij})_\alpha (\mathbf{f}_{ij})_\beta \right)$$

where \mathbf{f}_{ij} is the force on i due to j in unscaled form. These equations can be solved using a predictor-corrector technique or a scheme such as the Verlet 'velocity' algorithm.

In our simulations we integrated these equations of motion, allowing for changes in the system size in the x , y and z directions. The off-diagonal elements of the pressure tensor were not taken into consideration to allow for changes in the periodic box angles. Also, such a move is unphysical in the z direction since the confining surfaces have to remain parallel.

4.6.2 Integration of Equations of Motion

The above equations of motion (for the segment positions and the box velocities) were integrated using a Verlet-equivalent algorithm that stores positions, velocities and accelerations all at the same time and which minimizes the round off error¹³¹. This 'velocity Verlet' algorithm takes the form

$$\begin{aligned} \mathbf{r}(t + \delta t) &= \mathbf{r}(t) + \delta t \mathbf{v}(t) + \frac{1}{2} \delta t^2 \mathbf{a}(t) \\ \mathbf{v}(t + \delta t) &= \mathbf{v}(t) + \frac{1}{2} \delta t [\mathbf{a}(t) + \mathbf{a}(t + \delta t)] \end{aligned}$$

Earlier attempts to integrate the equations of motion using the Gear predictor-corrector algorithm were not successful. Using the predictor-corrector scheme always led to very large errors resulting in diverging values of conserved system variables such as energy. While the exact reason for this is unclear, here we suggest two explanations.

Firstly, our system consisted of molecules with chemical bonds, with a very high potential. When position coordinates are rescaled to account for the change in the periodic box dimensions, the Gear predictor-corrector algorithm, might have resulted in significant displacements of the bonded segments from each other, thus creating a very large error. Secondly, we used only one corrector step, as it is normally done in most Molecular Dynamics simulations, which may not have been sufficient due to the large errors generated. Consequently, the predictor corrector algorithm was unsuccessful in generating reliable trajectories. In short, the highly sensitive potential functions of bond lengths and bond angles may have resulted in very large errors in our calculation of trajectories when resizing of the periodic box was involved.

The velocity-Verlet scheme has presumably avoided this problem to a large extent since it just depended on a Taylor series expansion. Indeed, the trajectories generated using the velocity-Verlet scheme did not lead to a “blow-up” of the system with diverging energy values.

In the next section we discuss some of the simulations performed at solid-segment affinity values of 300.5K, 360.6K and 420.7K. In all these simulations the initial conditions were: a) periodic box size 9σ in x and y directions. b) 3 segmental layers wide in z direction. c) “piston” mass $Q = 40,000$ in MD units and d) isotropic pressure tensor π kept close to 0 bar.

4.6.3 Results and Discussion

In the isothermal-isobaric ensemble simulations an equilibrated system is expected to oscillate about some mean values of pressure and temperature. Conversely, the system

dimensions in the x, y and z directions should oscillate about some mean values. In figure 4.13, the average periodic box length in the x, y and z directions is shown as a function of time. The slit width in the z-direction always showed only small fluctuations around $\sim 4\sigma$. The periodic box sides in x and y directions never reach an equilibrium value around which they oscillate even after considerably long simulation steps. The longest simulation run for 800,000 time steps (~ 8 nsec) at $\epsilon_{sl} = 360.6K$ failed to show any trend towards an equilibrium. Our previous simulations under canonical ensemble conditions were only 2-4 nsec long.

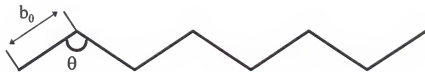
The calculation of the correlation functions also presented difficult problems. The pair correlation function calculates the probability of finding two segments separated by a certain distance. Sample pair correlation function curves at $\epsilon_{sl} = 300.5K$ and $360.6K$ are plotted in figure 4.14. No clear observations could be made from these plots. The rotational correlation function of the chain end to end vectors did not relax on the time scale of the simulations (figure 4.15). However, this data is not adequate to draw any conclusions on the behavior of the system, or the effect of ϵ_{sl} on the system behavior.

4.6.4 Conclusions

Molecular Dynamics simulations of n-octane films were attempted under isothermal, isobaric conditions. The isobaric conditions were simulated by allowing relaxation of the ensemble volume, via changing the box size. This study was unsuccessful due to the complexity of computing reliable segment trajectories. One reason for its failure could be attributed to the functional form of the bond length and bond angle potential functions, which could cause major errors with the scaling of periodic box size. Most of the

previous studies of NPT ensembles were on atomic systems where the chemical bonds were not present. Results obtained from the simulations performed were not always trustworthy since the system did not reach an equilibrium state. It was perceived prudent to abandon these simulations until more reliable methods for simulating NPT ensembles of molecules become available.

a)



b)

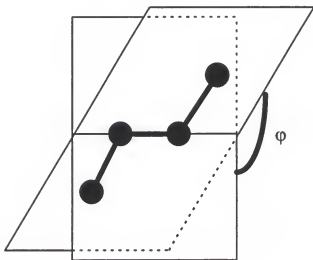


Figure 4.1. a) Sketch of a n-octane molecule skeleton. b) Illustration of the dihedral angle.

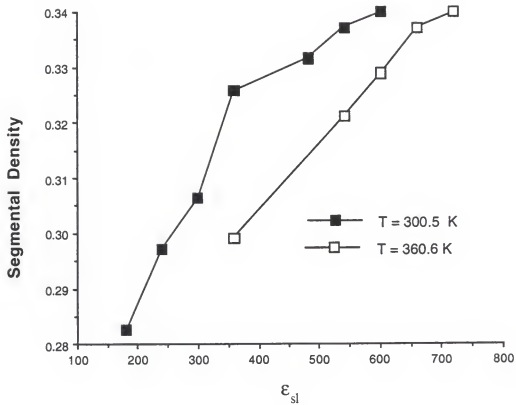


Figure 4.2. Average film density as a function of solid-segment affinity.

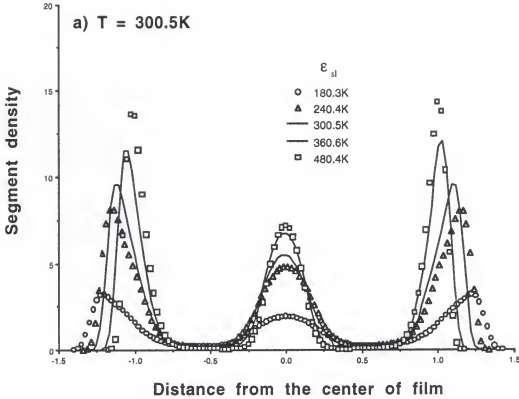


Figure 4.3: Segmental density profiles perpendicular to the solid surfaces. The distance on the x-axis is in molecular dynamics units. a) At $T = 300.5\text{K}$ for various values of ϵ_{sl} . b) At $T = 360.6\text{K}$ for various values of ϵ_{sl} . c) At $\epsilon_{sl} = 360.6\text{K}$ and $T = 360.6\text{K}$ for various values of pressure.

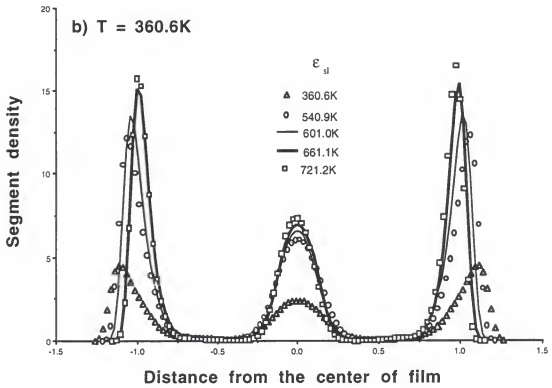


Figure 4.3 -- continued

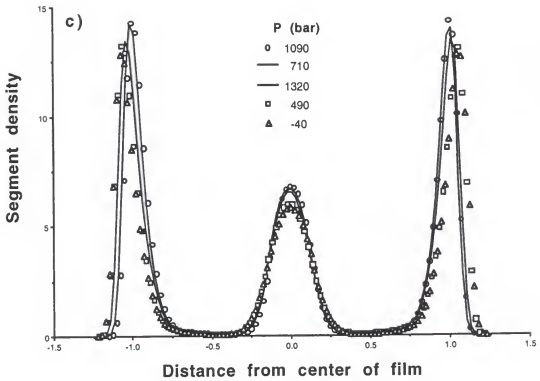


Figure 4.3 -- continued.

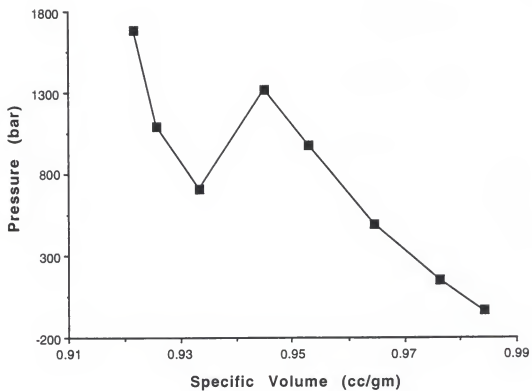


Figure 4.4. Pressure vs. Volume isotherm of the film at constant solid segment affinity.

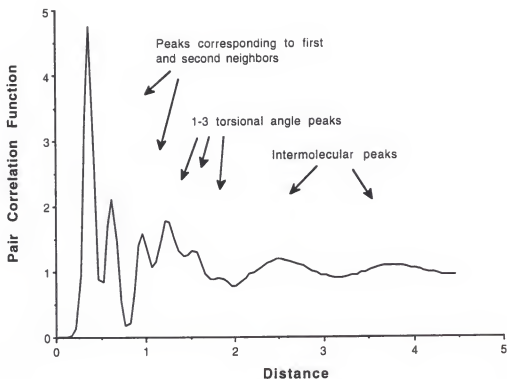


Figure 4.5. The typical shape of the pair correlation function curves. One unit of distance on the abscissa corresponds to one segmental diameter.

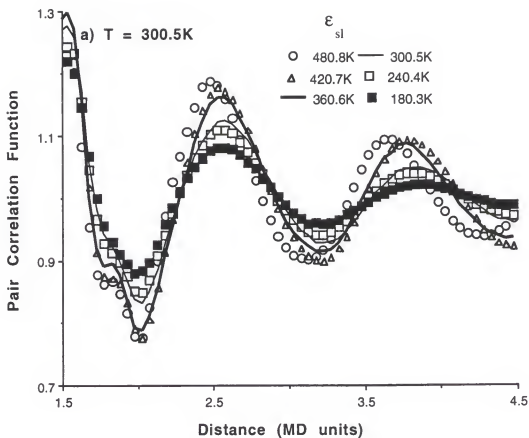


Figure 4.6. In-layer pair correlation function curves of the segments belonging to the first layer. a) At $T = 300.5\text{K}$ for several values of ϵ_{sl} . b) At $T = 360.6\text{K}$ for several values of ϵ_{sl} . c) At $\epsilon_{sl} = 360.6\text{K}$ and $T = 360.6\text{K}$ for several values of pressure.

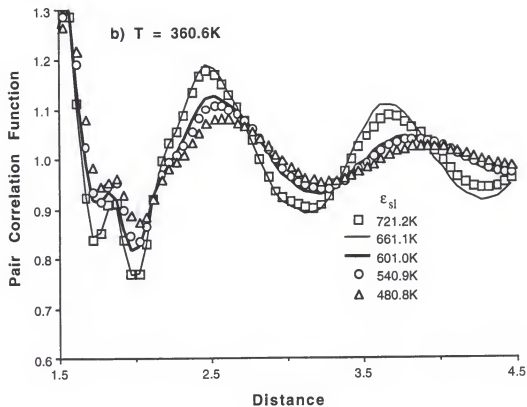


Figure 4.6. -- continued

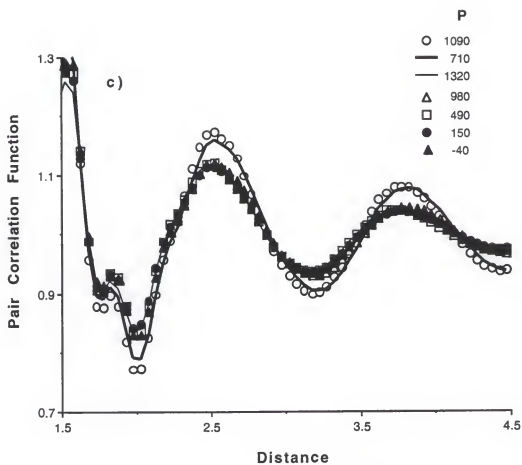


Figure 4.6. -- continued

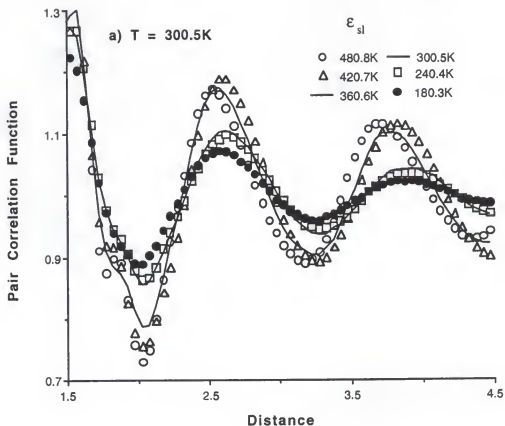


Figure 4.7. In-layer pair correlation function curves of the segments belonging to the middle layer. a) At $T = 300.5\text{K}$ for several values of ϵ_{sl} . b) At $T = 360.6\text{K}$ for several values of ϵ_{sl} . c) At $\epsilon_{sl} = 360.6\text{K}$ and $T = 360.6\text{K}$ for several values of pressure.

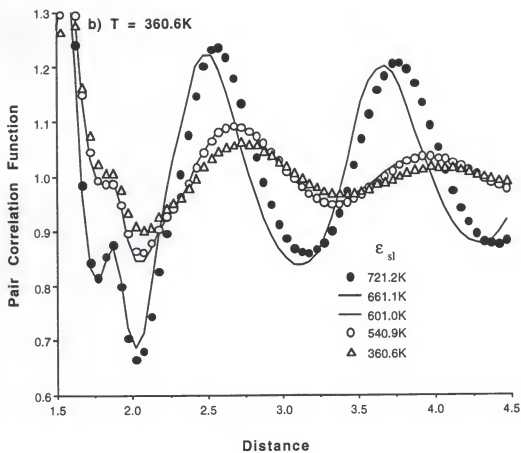


Figure 4.7. -- continued

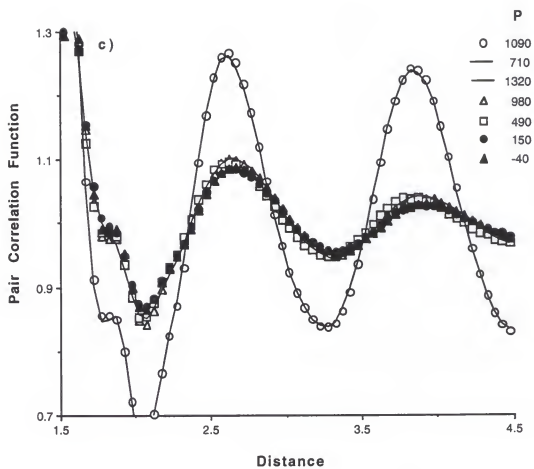


Figure 4.7. -- continued

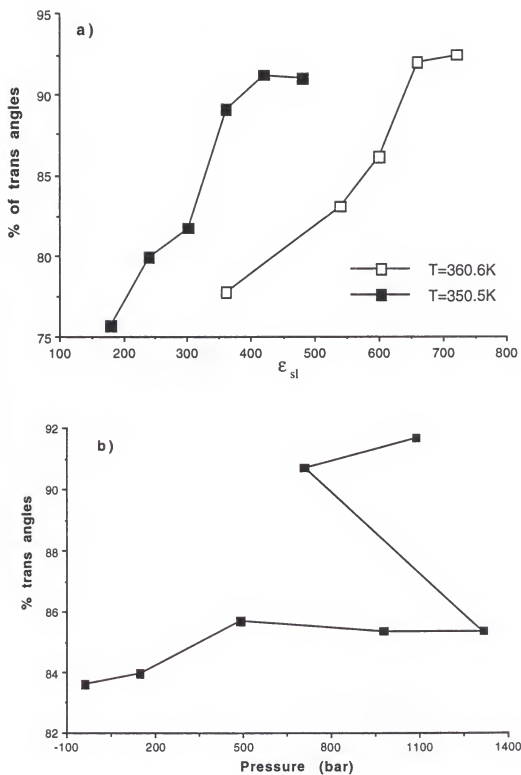


Figure 4.8. The percentage of trans angles as a function of a) solid-segment affinity b) pressure.

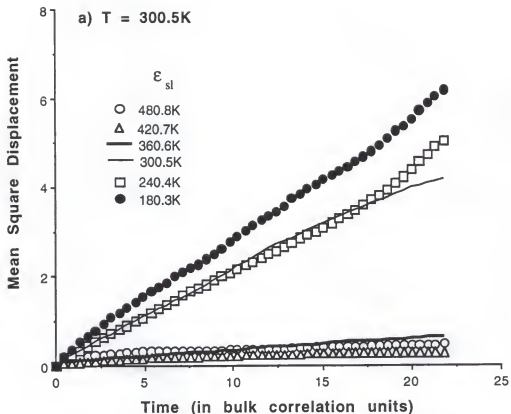


Figure 4.9. The average mean square displacement of chain centres of mass as a function of time. The time is scaled to the bulk correlation time and 20 units correspond to ~ 0.2 nsec. a) At $T = 300.5K$ for several values of solid-segment affinity b) At $T = 360.6K$ for several values of solid-segment affinity c) At $T = 360.6K$ and $\epsilon_{sl} = 360.6$ for several values of pressure.

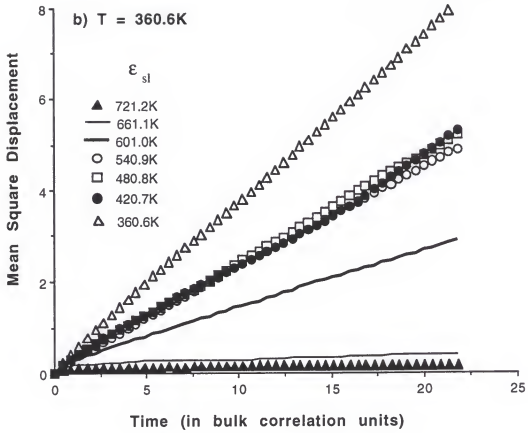


Figure 4.9. -- continued

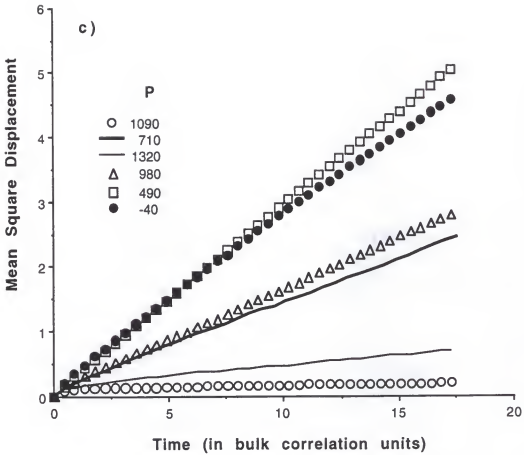


Figure 4.9. -- continued

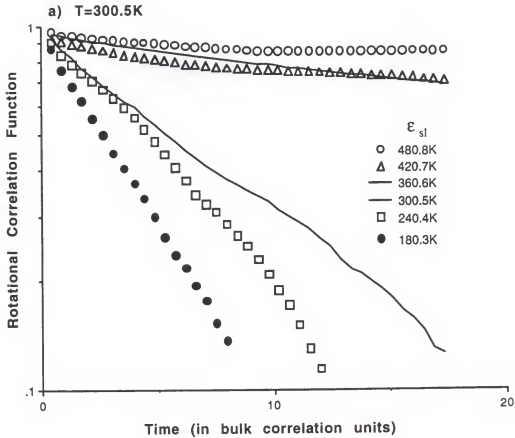


Figure 4.10. Rotational correlation function of the chain end-to-end vectors as a function of time. The time is scaled by the bulk correlation time. a) At $T = 300.5K$ for several values of solid-segment affinity b) At $T = 360.6K$ for several values of solid-segment affinity c) At $T = 360.6K$ and $\epsilon_{sl} = 360.6$ for several values of pressure.

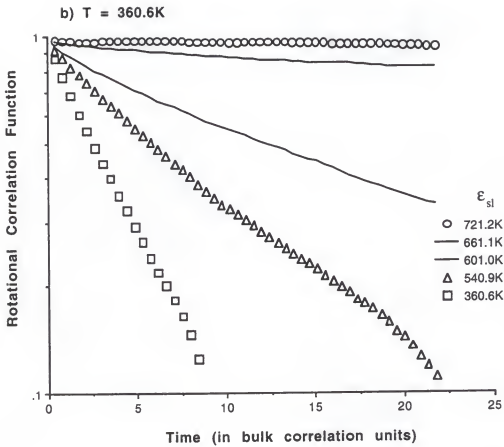


Figure 4.10. -- continued

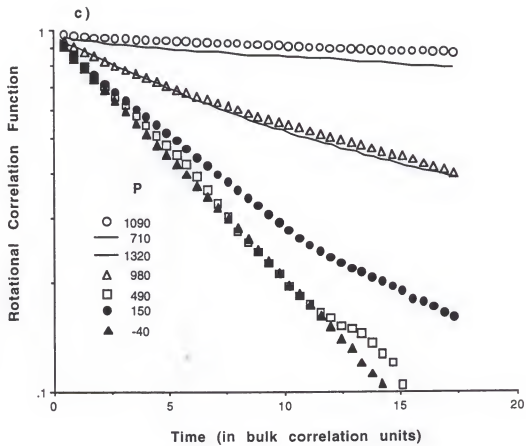


Figure 4.10. -- continued

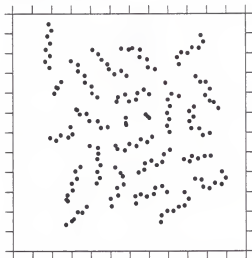
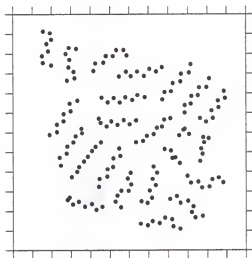
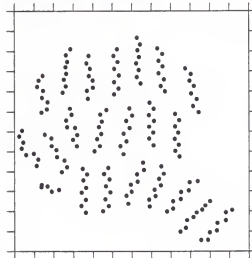
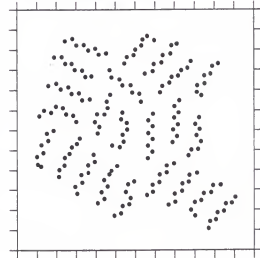
a) $\epsilon_{sl} = 180.3K$ b) $\epsilon_{sl} = 300.5K$ c) $\epsilon_{sl} = 360.6K$ d) $\epsilon_{sl} = 480.8K$ 

Figure 4.11. Typical "snapshots" of the first layer segments at several solid-segment affinity values at $T=300.5K$. The dots denote the projections of the centers of mass on the xy plane. The distance between the ticks correspond to one segmental diameter. a) and b) are below the transition threshold and c) and d) above the transition.

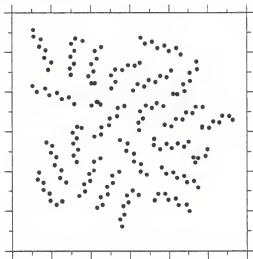
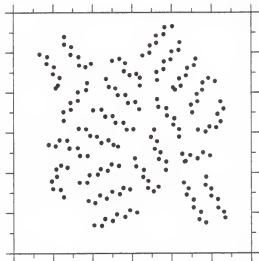
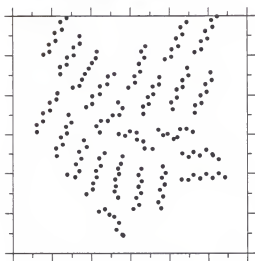
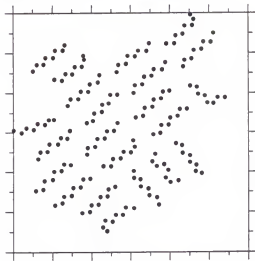
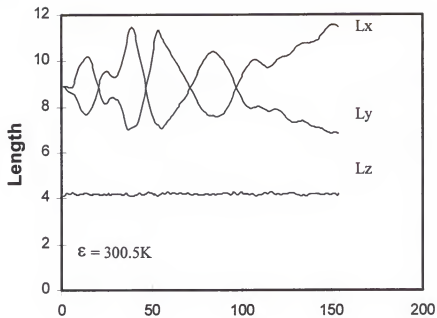
a) $P = -40$ bar**b) $P = 1320$ bar****c) $P = 710$ bar****d) $P = 1090$ bar**

Figure 4.12. Typical snapshots of the first layer molecules at different pressures. a) and b) are below the transition threshold and c) and d) above the threshold.

a)



b)

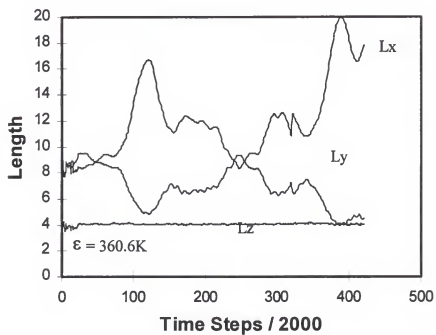


Figure 4.13: System size in the x, y and z dimensions. The periodic box sides (L_x and L_y) do not reach an equilibrium value.

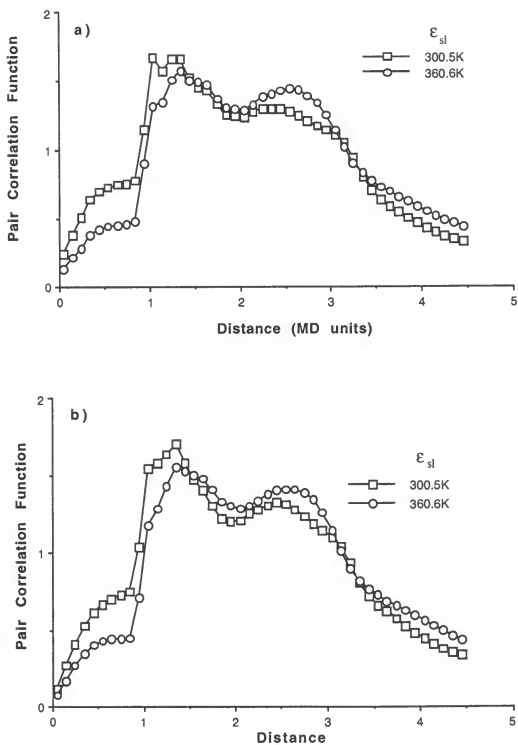


Figure 4.14. In layer pair correlation function curves for the simulations performed in the isothermal-isobaric ensemble. a) First layer b) Middle layer.

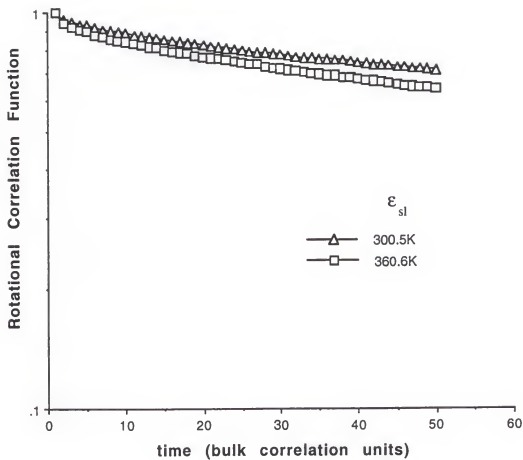


Figure 4.15. Rotational correlation function of the chain end to end vector, for the simulations under isothermal-isobaric ensemble conditions.

CHAPTER 5

SIMULATIONS OF SOLID PARTICLE-POLYMER SOLUTION INTERFACES

5.1 Introduction

In this chapter we discuss our simulation studies of the interface between a solid particle surface and dilute polymer solution at theta conditions. The interface at good solvent conditions has been studied in our group. In section 5.2 the model of polymer chains next to surfaces employed is discussed. The algorithms employed for simulation are presented in section 5.3. Section 5.4 presents the way theta solvent conditions are determined for our system. In section 5.5, the details of systems simulated at various concentrations, surface energies and chain lengths are given. Section 5.6 contains the first results of the simulations and a discussion of these results. The findings of this study are presented in section 5.7 and the future directions for this work are briefly discussed in section 5.8.

5.2 Model Description

The polymer chains in our simulations are modeled as self avoiding walks on a cubic lattice. These walks were confined between two well-separated flat impenetrable solid surfaces. Figure 5.1 shows a two dimensional lattice schematic of a solid surface-polymer chain interface. The modeling of polymer chains as self avoiding walks on a cubic lattice is adequate for our purposes to analyze the large scale conformational features of the chain⁸. A more detailed and segmental level of modeling would have been

computationally extremely intensive with marginal gain in the accuracy of the properties computed¹⁰⁷.

Simulating the interface between a solid particle surface and a semi infinite polymer solution with the available tools presents a difficult computational challenge. This problem is circumvented by simulating polymers in solution between two well-separated flat surfaces. The separation between the surfaces was large enough to maintain a bulk-like concentration of segments in the mid portion of the gap. The study of this system yields better statistics since each simulation is equivalent to simulating two solid surfaces in equilibrium with the bulk polymer solution.

In each of the systems studied the polymer chains were monodisperse, and the number of chains and the surface-segment interaction energy were fixed. These simulations correspond to canonical ensemble conditions.

The solvent conditions were set to theta solvent conditions, i.e., the single chain statistics in bulk solution are Gaussian. The method of determination of theta conditions is discussed in a separate section below.

We studied solid surfaces with two different surface-segment interaction energies (E_s). The first surface has a physisorption energy of $E_s = -0.5kT$ and the second has a higher physisorption energy with $E_s = -0.7kT$. The first layer, consisting of the train segments has a very low density (smaller than the bulk density) when the solid surface is repulsive or non-adhesive. At the threshold adsorption energy $E_s^* \approx -0.3kT$, the loss of the entropic contribution to the polymer chain free energy is compensated by the gain in the surface adhesive energy and the first layer segment density is equal to the bulk

density. Under constant bulk conditions, the first layer segment concentration quickly reaches an asymptotic limit (close to a melt-like density), with the increase in the surface physisorption energy. Attempts to simulate dilute solution-solid surface interfaces at an adsorption energy of $E_s = -1kT$ always led to the irreversible adsorption of the polymer chains. Hence we chose two values of adsorption energy ($-0.5kT$ and $-0.7kT$), that were between the threshold and $E_s^* = -0.3kT$ and $E_s = -1kT$.

5.3 Methodology

Monte Carlo methods are best suited to study our system of interest. Configurational Bias Monte Carlo (CBMC) moves and simple Lattice Monte Carlo (LMC) moves are chosen to simulate our system of interest. CBMC has the capacity to overcome very high kinetic barriers. Even the most tightly adsorbed chains desorb on the length of simulations when CBMC was used. LMC moves mimic physical behavior of the polymer chains. Hence a combination of CBMC and LMC schemes is expected to explore the configuration space more effectively. In the simulations at $E_s = -0.5kT$ only CBMC moves were used. The second set of simulations at $E_s = -0.7kT$ were performed using a combination of CBMC and LMC moves.

In order to obtain valid statistics of system properties, it is important to use configurations well decorrelated from each other. For CBMC moves, the sampling interval between configurations used for averaging properties allowed sufficient number of successful moves to change the configurations of all the chains at least once on average. In a similar fashion, sufficient number of LMC moves were performed to allow the complete relaxation of the end to end vectors of all the chains in the system.

The preparation of the initial configuration was done by using the method proposed by Kolinski et al¹¹⁴. The algorithm consists of placing initial segments on a lattice and then growing the chains to the desired length. Partially grown chains are periodically subjected to LMC moves (explained in the next section) to equilibrate the growth of the chains. This equilibration step is particularly helpful in generating highly dense configurations and very long chains.

5.3.1 Simple Lattice Monte Carlo Algorithm

LMC moves constitute of end segment rotation, normal jumps, crankshaft rotation and reptation. These moves can be easily understood with the help of Figure 5.2. After each LMC move, the energy of the new trial conformation E_{trial} , is compared with the old conformation energy E_{old} . The new conformation is accepted with a probability of $\exp(E_{\text{trial}}/E_{\text{old}})$.

5.3.2 Configurational Bias Monte Carlo Algorithm

CBMC^{132, 133} is an effective method to simulate reasonably long polymer chains (up to 300 segments). This method explores the phase space of the system configurations by allowing unphysical changes in the polymer conformations. Due to its design, this method can explore the configuration space of a multi-chain system very effectively and can overcome high energy barriers in a relatively short simulation.

The algorithm for CBMC method as applied to our system of chains is as follows:

- Consider a system of polymer chains confined between two flat impenetrable surfaces.
- Choose one polymer chain randomly.

- Randomly select a segment on this chain. (In our simulations at $E_s = -0.7kT$ we select the segment with a probability distribution that is parabolic, i.e., the probability of selecting a chain segment in the middle is higher than choosing the end segments. This modification does not effect the principle of detailed balances and microscopic reversibility and hence is valid. Also, this modification ensures that the majority of the successful chain growths will result in a significant change in the overall chain conformation, thereby exploring the conformational phase space more efficiently.)
- Snip the chain at this point and discard either one of the portions.
- Attempt to regrow the chain to its original length using Rosenbluth's self avoiding walk algorithm. The probability of growing into a particular neighboring site is computed as

$$P_j = \frac{B_j}{\sum_{j=1}^n B_j} \quad (5.1)$$

where B_j is the Boltzmann weight of site j and n is the number of neighboring lattice sites. Determine the Rosenbluth weight of the trial configuration, W^{trial} . The weight W_{m+1} after each growth step is computed using the following formula:

$$W_{m+1} = W_m \frac{\sum_{j=1}^n B_j}{n} \quad (5.2)$$

Here W_m is the Rosenbluth weight associated with the growth of m segments. W_1 is set to unity.

- Compare the trial configuration weight to the original configuration weight, W^{old} and accept or reject this move based on the criteria $W^{\text{old}}/W^{\text{trial}} < \text{Random}[0,1]$, where $\text{Random}[0,1]$ is a random number between 0 and 1.

5.4 Determination of Theta Solvent Conditions

In a theta solvent, the polymer chains follow Gaussian conformational statistics. In general, the radius of gyration R_g and the magnitude of the end to end vector R scale as N^ν , where N is the number of segments in the chain. The exponent ν is 0.59 for polymer chains that follow self avoiding random walk statistics (good solvent conditions). When polymer chains follow random walk (ideal chain) statistics in theta solvents, as in this study, ν is 0.5. To examine the interface of solid surfaces and polymer solutions under theta conditions, it is necessary to ensure that polymer chains follow Gaussian statistics in the bulk phase.

The theta solvent condition can be understood as the solvent molecules exerting a mild repulsive force on the polymer segments and compressing the chain. This can be equivalently treated as the polymer segments exerting an attractive force on the neighboring segments and thereby compressing the chain. The Flory-Huggins χ parameter characterizes the solvent quality and is given by the formula

$$\chi = 0.5(2\chi_{sp} - \chi_{ss} - \chi_{pp}) \quad (5.3)$$

where χ_{ss} is the interaction parameter between solvent molecules, χ_{pp} is between polymer segments and χ_{sp} is between a solvent molecule and a polymer segment. For good solvents, $\chi < 0.5$ and $\chi = 0.5$ corresponds to theta solvent conditions.

The interaction parameter χ_{pp} is related to the potential energy of interaction between the sites through the following formula:

$$\chi_{pp} = \frac{z\epsilon_{pp}}{kT} \quad (5.4)$$

Here ϵ_{pp} is the potential energy of interaction between two polymer segments, z is the lattice coordination number, k is the Boltzmann constant and T is the temperature of the system. For a cubic lattice, $z = 4$. We set ϵ_{ps} and ϵ_{ss} to zero to evaluate the net segment-segment interaction energy that would yield Gaussian chains. It is clear from equations 3 and 4 that $\epsilon_{pp} = -0.25kT$ for theta solvent conditions. Simulations with ϵ_{pp} close to $-0.25kT$ are hence expected to study Gaussian chains.

We have simulated single chains of various lengths in large periodic boxes to determine the value of ϵ_{pp} corresponding to theta conditions. The details of the systems studied are given in Table 5.1.

Table 5.1. Simulation parameters of single chain systems to determine theta solvent ϵ_{pp}

Chain Length	Periodic Box size	Number of Steps
20	15	100,000
40	20	100,000
60	30	150,000
100	40	150,000
200	50	200,000
300	70	500,000

The radius of gyration and the end to end distance are plotted as a function of chain length in Figure 5.3 for the various ϵ_{pp} studied. A power law curve fit to these curves gives us the value of the exponent ν . Figure 5.4 is a plot of the values of ν as a function

of the segment-segment interaction energy ϵ_{pp} . The value of ν remains close to 0.6 as the value of ϵ_{pp} decreases from 0 to $-0.2kT$. As ϵ_{pp} decreases to $-0.25kT$, ν suddenly drops to values close to 0.5. The value of ν is observed to be 0.5015 at $\epsilon_{pp} = -0.26kT$.

In all our studies of solid-polymer interfaces we have used the value of $\epsilon_{pp} = -0.25kT$ to simulate theta solvent conditions. This is a good choice since the exponent $\nu = 0.5$ corresponds to the limiting case of very long chains. Since our data includes chain lengths up to 300 segments only, we obtain a slightly lower segment-segment interaction energy. Considering that the Flory-Huggins theory is not an exact theory and the parameter χ is not rigorously given by equations 5.3 and 5.4, the close agreement we find with the theoretical prediction is remarkable.

5.5 System Description

We performed two series of simulations to study the solid-theta solvent polymer solution interfaces. In the first series of simulations, the solid surface attractive potential was set to $E_s = -0.5kT$. Polymer chains that are 40, 60, 100, 200 and 300 segments long were simulated at several bulk concentrations. The second set of simulations was at $E_s = -0.7kT$. At this surface potential chains that are 50, 100 and 200 segments long are investigated at dilute and semi-dilute concentrations. The details of the systems studied are given in Table 5.2.

Table 5.2: Simulated systems

Surface-Segment Energy (E_s)	Chain Length (L)	Bulk Densities (ρ)	System Size ($L_x=L_y, L_z$)	CBMC moves	LMC moves
-0.5	60	3.35E-4, 4.99E-3, 1.27E-2, 2.28E-2, 3.58E-2, 4.89E-2	40, 50	10E+6	0
	100	3.28E-6, 9.91E-6, 2.00E-5, 7.34E-5, 1.29E-4, 2.51E-4	100, 120	50E+6	0
	200	7.66E-7, 5.45E-7, 5.53E-6, 9.32E-6, 4.07E-5, 2.25E-4	100, 100	75E+6	0
	300	3.77E-5, 1.30E-4, 4.50E-4, 1.14E-3, 2.29E-3	100, 100	100e+6	0
-0.7	50	3.53E-6, 6.02E-5, 6.48E-4, 3.26E-4, 1.67E-2, 2.53E-2	30, 50	15E+6	15E+8
	100	1.27E-4, 1.26E-3, 1.10E-2	40, 70	30E+6	30E+8
	200	4.76E-4, 3.57E-3, 9.10E-3, 3.19E-2	50, 100	50E+6	50E+8

5.6 Results and Discussion

Figure 5.5 shows a typical segment density profile between the confining solid surfaces at $E_s = -0.7kT$ and $L = 50$. The overall segment density is higher at the solid surface and flat in the mid portion of the gap. From this plot we infer that our simulated systems were large enough to mimic a solid particle surface in contact with a semi-infinite bulk polymer solution.

In figure 5.6, the interfacial or the first layer segment density is plotted as a function of the bulk concentration for the two surface energies studied. In these adsorption isotherms, the first layer segment density increases with the bulk concentration for all the

chain lengths. The adsorbed layer density reaches an asymptotic limit with increasing bulk concentration. Also, lower chain lengths occupy a smaller fraction of the surface area than higher chain lengths. From this observation one can infer that, long chains are more likely to be adsorbed on a physisorbing surface than short chains.

The conformational features of chains at an interface can be understood by examining the tail, train and loop size characteristics. Trains are sequences of segments that are in contact with the surface. Segments that connect two consecutive trains constitute a loop and the free ends of the chain are termed as tails. An adsorbed chain may have 0, 1 or 2 tails.

The average tail length for various chain lengths is plotted in figure 5.7 as a function of the bulk concentration. Clearly, the average tail size increases with increasing bulk concentration. The average tail size also increases with increasing chain length as expected. Figures 5.8 and 5.9 show the average loop and train sizes as a function of bulk concentration. The average loop size increases with increasing bulk concentration, similar to the average tail size. The average train size shows the opposite trend, a decrease in its size with increasing bulk concentration. From figures 5.7, 5.8 and 5.9, it is clear that chains are tightly adsorbed with long trains and short tails and loops at low bulk concentrations and are loosely pinned with short trains and long tails and loops at higher bulk concentrations. These facts together with the observation in figure 5.6, show that more chains adsorb with short trains at high concentrations and fewer chains with long trains at low bulk concentrations.

In chapter 2 we have discussed the self consistent mean field theory of Semenov and his coworkers. Using the ground state dominance approximation, for the extremely dilute concentration limit, the limiting form of the overall concentration profile, in the loop dominant region was shown to be

$$\varphi(z) = \frac{2}{(z+b)^2} \quad (5.5)$$

where z is the distance from the surface and b is related to the surface segment interaction energy. When the bulk concentration $\varphi_0 \rightarrow 0$, the adsorbance Γ is given by

$$\Gamma = \int_0^{\infty} \varphi(z) dz \quad (5.6)$$

In our case where we employ a lattice model, we can estimate b , by using equation 6 and evaluating it in some interval $[1, k]$, where k is a large number. When k is very large,

$$\Gamma \approx \frac{2}{1+b} \quad (5.7)$$

or

$$b = \frac{2}{\Gamma} - 1 \quad (5.8)$$

When $E_s = -0.5kT$, using the simulation data of polymer chains 300 segments long, at the bulk concentration of $3.77e-5$, the estimate yields $b = 0.9$. The estimated value of b decreases with the increase in bulk concentration. We can safely predict that $b > 0.9$ for our systems simulated at $E_s = -0.5kT$. Similarly, estimates for systems simulated at $E_s = -0.7kT$ and chain length 200 predict $0.25 < b < 0.67$. In the analysis of data that follows we have used the values of $b = 0.9$ for $E_s = -0.5kT$ and $b = 0.46$ for $E_s = -0.7kT$.

The mean field theory by Semenov and coworkers predicts the limiting functional form of the segment concentration profiles due to tails and loops for very long chains.

Only for chains that are over 100,000 segments long can the proximal, intermediate and distal interfaces be clearly delineated. For chain lengths simulated in our work, the intermediate regime is ill defined. Hence we compare our results only in the proximal and distal regimes of the polymer interface at very dilute and dilute concentrations.

The predictions of Semenov and workers were summarized in Chapter 2. Here, the functional forms of these scaling laws are summarized for the proximal and distal interface. In Semenov's work the distance z is considered to be much larger than the parameter b . However, in our simulations of relatively small chain lengths, the parameter b cannot be neglected from these laws since the magnitude of z is comparable to b , at least in the proximal region.

$$\varphi_i = \frac{2}{(z+b)^2} \quad \varphi_i = \frac{4z}{(z^*)^3} \ln\left(\frac{z^*}{z}\right) \quad b < z \ll z^* \quad (5.9)$$

$$\varphi_i \sim \frac{(z^*)^6}{\lambda^8} e^{-2(z+b)/\lambda} \quad \varphi_i \sim \frac{1}{\lambda^2} e^{-(z+b)/\lambda} \quad \lambda \ll z \ll D \quad (5.10)$$

Figure 5.10 shows a schematic of the concentration profiles of a solid-dilute polymer solution interface. The overall segment concentration is expected to decrease with an exponent of z^{-1} , close to the surface when the solution is semi-dilute. A small depletion zone is predicted by theory at a distance $\approx R^2/\lambda$. The loop segment concentration decreases monotonically as one moves away from the surface, while the tail segment concentration initially increases before decreasing. Now, we compare these observations with our simulation results. Figures 5.11a and 5.11b show the typical concentration profile of segments and the contributions from segments belonging to loops, tails and free chains at dilute concentrations. The overall concentration steadily decreases as the

distance from the solid surface increases. A faint depletion zone is observable in Figure 5.11a, but is not present in figure 5.11b.

Before the point z^* , loop segments are the dominant contributors to the overall concentration. Beyond z^* , the concentration is mostly due to tail segments. As we approach the bulk region, segments belonging to the free chains contribute to the concentration with negligible or no contribution from adsorbed chain segments.

We now compare the functional forms of the overall, loop and tail density profiles with the theoretical predictions in the proximal and distal interfaces. Due to the limited chain lengths that can be simulated (up to 300 segments) the intermediate regime cannot be clearly distinguished in our simulations. Since the theoretical predictions are for the very long chain limit and very dilute concentrations, we should expect that our results do not agree completely with the theory. However, the general trends of the concentration profiles should show a trend towards the theoretical limit.

5.6.1 Proximal Regime

5.6.1.1 Overall concentration profile

According to the scaling prediction of de Gennes, the overall segment concentration close to the wall should decay as z^{-1} when the bulk solution is semi-dilute. As the bulk concentration decreases, this exponent is supposed to decrease to values less than -1. In the limit of infinite dilution, the concentration profile would decay as $(z+b)^{-2}$. In figures 5.12a and 5.12b, the overall segment density profiles in the proximal region are plotted as a function of $z+b$ for various bulk concentrations. Using a least squares power law curve fit to this data we see that the exponent decreases from -1.47 to -2.04 as the bulk

concentration decreases from $2.29\text{E-}3$ to $3.77\text{E-}5$ when $E_s = -0.5\text{kT}$ and $L=300$. Similarly when $E_s = -0.7\text{kT}$ and $L = 200$, the power law fits show that as the concentration decreases from $3.19\text{E-}2$ to $4.76\text{E-}4$ the exponent decreases from -1.23 to -1.85 . The data demonstrates that the ground state dominance approximation holds true as the bulk concentration $\phi_0 \rightarrow 0$.

5.6.1.2 Loop concentration profile

In the proximal interface loops are dominant. From equation 5.9 the loop segment concentration is expected to decay with an exponent of -2 . In figures 5.13a and 5.13b we examine the power laws followed by the loop segments as a function of $z+b$ for the simulated systems. When $E_s = -0.5\text{kT}$ and -0.7kT the exponent increases from -2.3 to -1.9 as the bulk concentration increases. Clearly, the loop segment concentration profiles follow the mean field theoretical predictions for the longest chain lengths simulated.

5.6.1.3 Tail concentration profile

The tail concentration is expected to increase approximately linearly close to the solid surface. However, owing to the short range of this increase for the chain lengths simulated no quantitative comparison can be made. From figure 5.14 we can comment that the tail concentration in the proximal regime shows the same qualitative trend as in figure 5.10. The maximum shifts to the right as the bulk concentration increases.

5.6.2 Distal Regime

The concentration of segments belonging to loops and tails should decrease exponentially in the distal regime, where the tail segments are the major contributors to the overall concentration.

In figure 5.15 loop segment concentration profiles in the distal regime are plotted for the two systems studied. Figure 5.16 contains the tail segment profiles in the distal regime. These concentration profiles show very clear exponential decay. The exponents of decay for the loop and tail segment profiles are predicted to differ by a factor of 2 (Equation 5.10) in the long chain limit. In our data we see that the ratio is ~ 2.3 at $E_s = -0.5kT$ and ~ 2.5 at $E_s = -0.7kT$, which is in very good agreement with the theoretical value.

5.7 Summary and Conclusions

In this study we have examined the interface between a solid particle surface and dilute neutral polymer solution under theta conditions. Monte Carlo simulations using both Configurational Bias Monte Carlo and simple Lattice Monte Carlo moves were made of this system for two different solid surface-polymer segment energies. We have shown that longer polymer chains tend to adsorb more tightly, with more surface coverage on the solid surface than shorter chains. The chains are tightly adsorbed, at low bulk concentrations. The increase in the bulk concentration results in more chains adsorbing loosely on the surface with shorter trains and longer loops and tails.

Our simulations studied chain lengths of up to 300 segments long. The study of these chains is of practical interest since most polymer dispersants used to stabilize colloidal

suspensions are 100-300 statistical segments long. The recent two order parameter approach of Semenov and coworkers treats the solid-polymer solution interface for very long chains ($N > 10^5$). Only at very high chain lengths can the interface be clearly distinguished into proximal, intermediate and distal regimes. In our simulations the intermediate regime is ill defined. We compared the functional forms of the segment density profiles due to tails and loops in the proximal and distal regimes. Our results show good agreement with the theoretical predictions and exponents show the correct asymptotic trend with increasing chain length. In the proximal interface the overall segment density decreases as z^{-2} in the infinite dilution limit and changes towards z^{-1} as the bulk concentration approaches semi-dilute conditions.

These simulation studies provide quantitative data on polymer chains of intermediate lengths, which cannot be treated by the theory easily. These simulations also confirm the validity of the recently developed self consistent mean field theory by Semenov and coworkers at theta solvent conditions.

5.8 Future Directions

Interfacial polymer simulation is a very fertile area with many complicated and challenging problems. This is partly due to the large number of factors associated with a polymeric interfacial system (chain lengths, chemical composition, surface properties, thermodynamic conditions, polydispersity etc.) and partly due to the complexity of the system, which is not easily amenable to theory. Among the several unresolved problems of polymeric interfaces, two problems are natural extensions of the current work.

5.8.1 Particle-Bidisperse Polymer Solution Interface

In industrial situations, the polymeric dispersants are not monodisperse but contain a range of molecular weights. From our study of monodisperse systems we can indirectly conclude that the longer polymer chains adsorb on the solid surface, displacing the shorter chains into the bulk. Simulating a bidisperse system can directly determine this. Furthermore, studying such a system offers direct insights into systems encountered in industrial situations.

5.8.2 Particle-Polyelectrolyte Solution Interface

Polyelectrolytes are frequently used as suspension stabilizers since they provide an electrostatic repulsive barrier in addition to the steric repulsion. Simulating such a system is not an easy task since the electrostatic interactions are long range. Most studies of particle-polyelectrolyte interfaces have been experimental and theoretical. There are few simulation studies of adsorbed polyelectrolytes from solution. The simulation studies have so far treated single chains in bulk solution. Simulation studies of polyelectrolyte systems is an area with numerous issues that are still not explored.

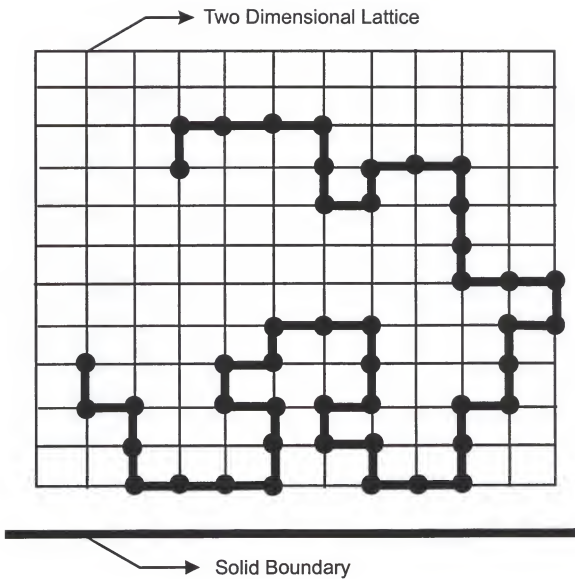


Figure 5.1. Schematic of a polymer chain on a two dimensional square lattice, constrained by a solid boundary.

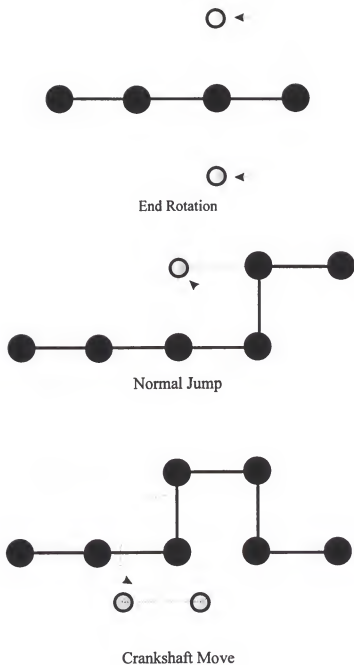


Figure 5.2. Schematic illustration of end bead rotation, normal jump and crankshaft moves.

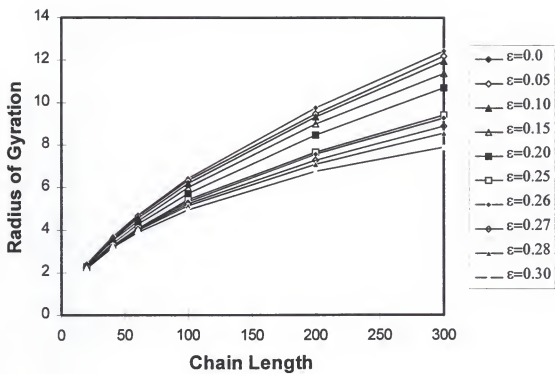


Figure 5.3. The radius of gyration of a single chain as function of chain length at several solvent conditions.

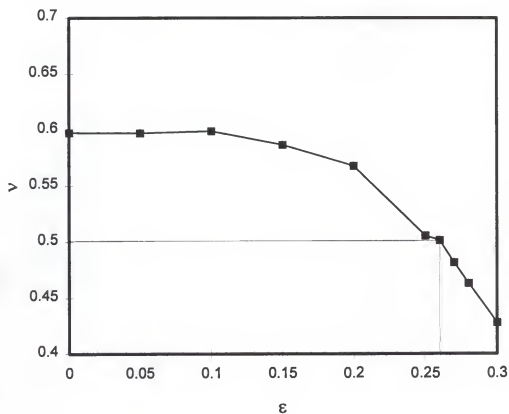


Figure 5.4. The exponent ν as a function of the segment-segment interaction potential ϵ .

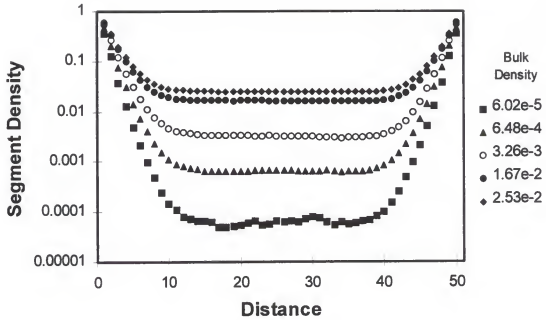
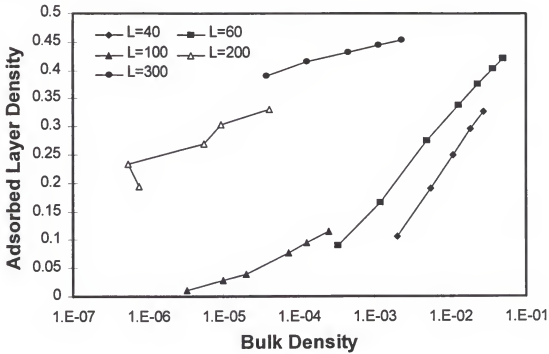


Figure 5.5. Typical segment density profiles between the two surfaces. Here the two confining surfaces are at 0 and 51. The chains in this system are 50 segments long and the surface-segment potential is $E_s = -0.7kT$.

a) $E_s = -0.5kT$



b) $E_s = -0.7kT$

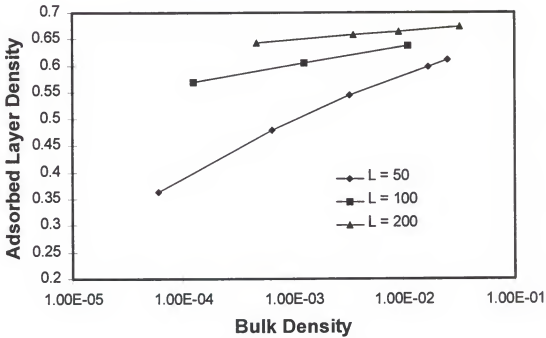


Figure 5.6. The density of the adsorbed segments (first layer) as a function of the bulk concentration at a) $E_s = -0.5kT$ and b) $E_s = -0.7kT$.

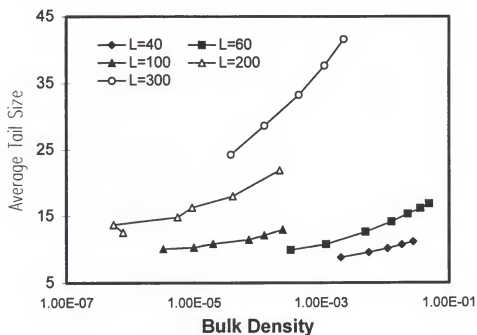
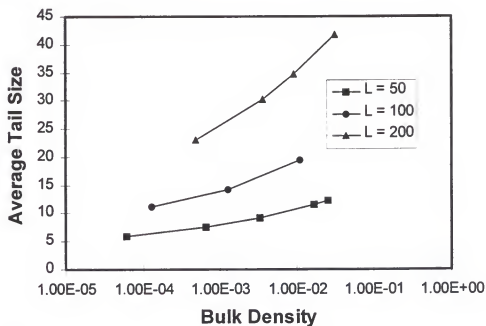
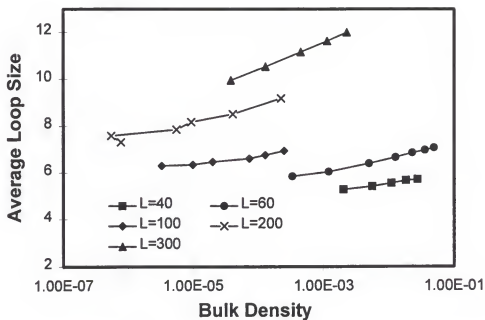
a) $E_s = -0.5kT$ b) $E_s = -0.7kT$ 

Figure 5.7. Average tail size as a function of the segment bulk concentration. The tail size increases with increasing bulk concentration.

a) $E_s = -0.5kT$



b) $E_s = -0.7kT$

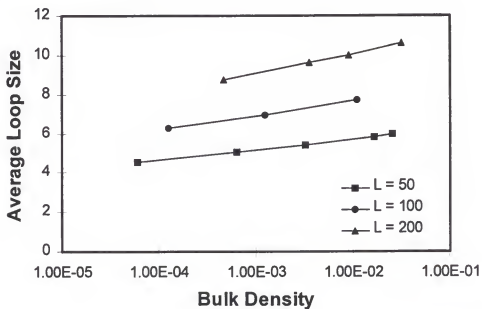


Figure 5.8. Average loop size as a function of the bulk segment density. The loop size increases with the bulk density.

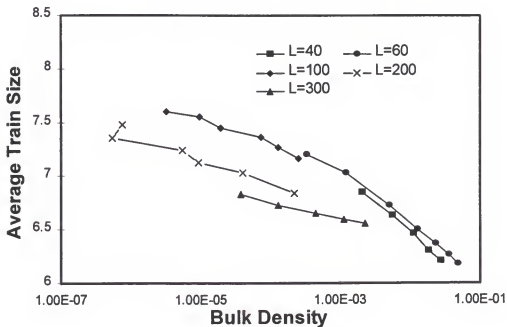
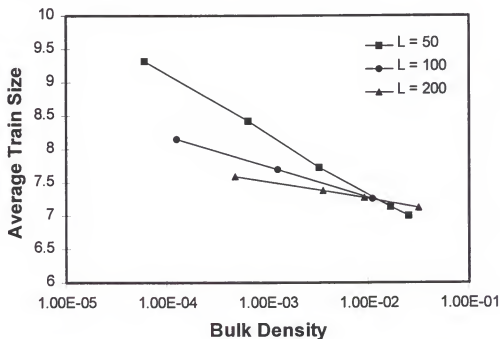
a) $E_s = -0.5kT$ b) $E_s = -0.7kT$ 

Figure 5.9. Average train size as a function of the bulk segment density. The trains become shorter with increasing concentration. Also, the average train size is comparable for all the different chain lengths.

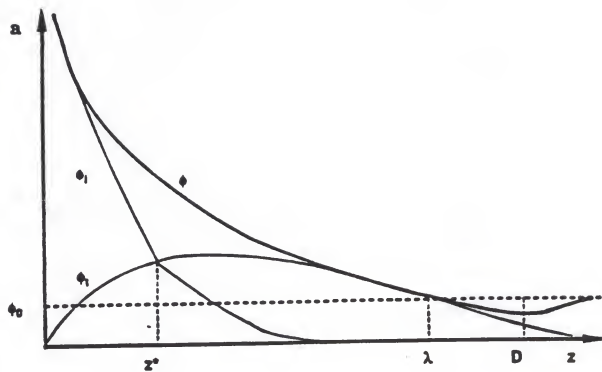
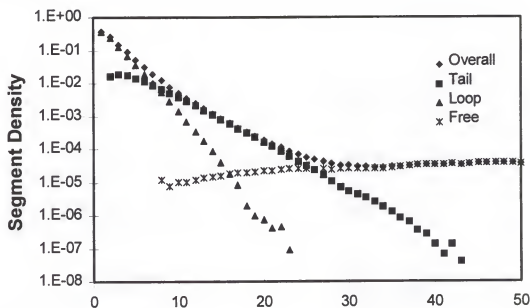


Figure 5.10. Schematic of the segment density profile at the interface between an attractive solid surface and a dilute polymer chain solution.

a) $E_s = -0.5kT$, $L = 300$, $\rho = 3.77E-5$



b) $E_s = -0.7kT$, $L = 200$, $\rho = 4.76E-4$

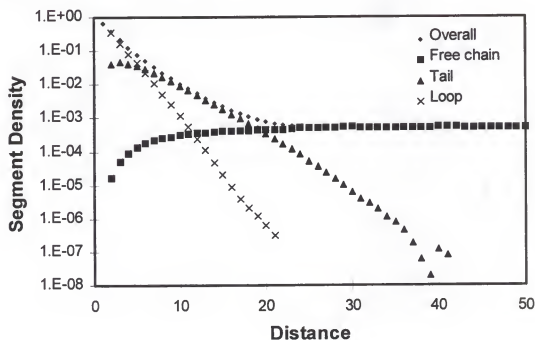
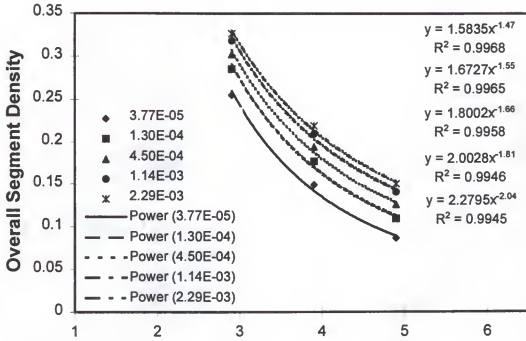


Figure 5.11. Segment density as a function of the distance from the wall. The overall segment density is the sum of the densities due to free chain segments, tail segments and loop segments.

a)



b)

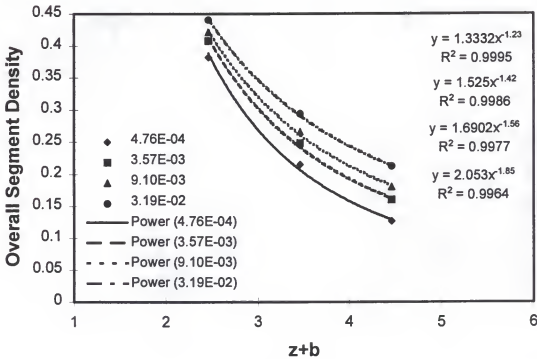
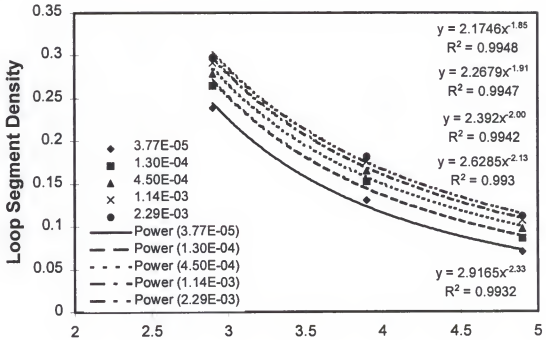


Figure 5.12: Overall concentration profile close to the wall, and power law curve fits for
a) $E_s = -0.5kT$ and $L = 300$ b) $E_s = -0.7kT$ and $L = 200$.

a)



b)

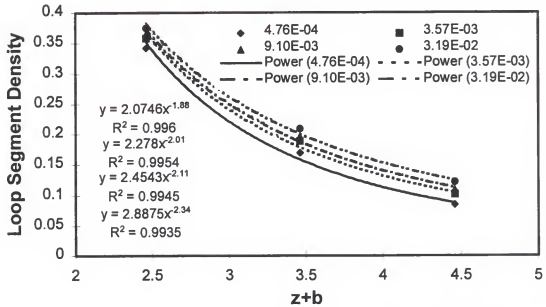


Figure 5.13. Loop segment density in the proximal interface. The power law curve fits and the corresponding equations are shown. a) $E_s = -0.5kT$, $L = 300$, b) $E_s = -0.7kT$, $L = 200$.

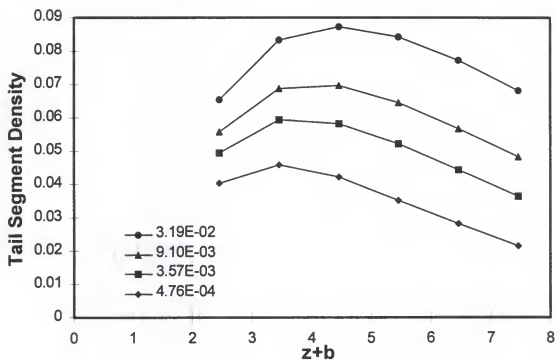
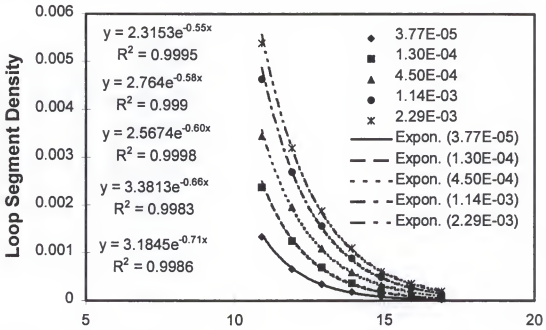


Figure 5.14. Tail segment density in the proximal interface at $E_s = -0.7kT$ and $L = 200$. The concentration goes through a maximum which shifts to the right with increasing bulk concentration.

a) $E_s = -0.5kT$, $L = 300$



b) $E_s = -0.7kT$, $L = 200$

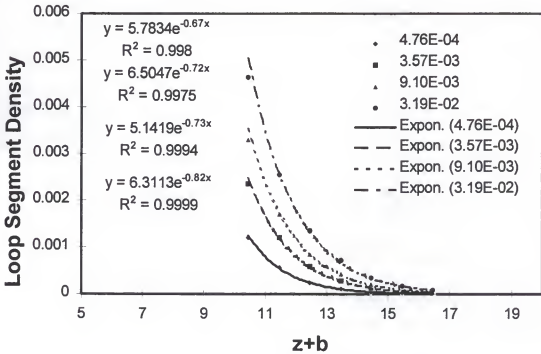
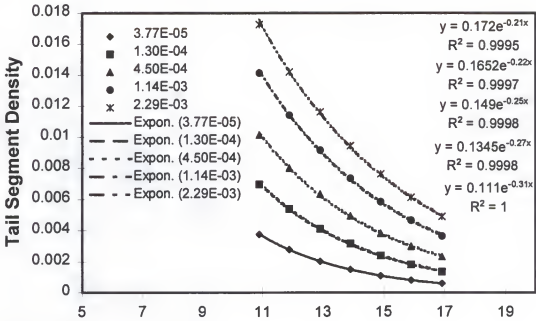


Figure 5.15. Loop segment density profile in the distal regime. The profile shows exponential decay.

a) $E_s = -0.5kT$, $L = 300$



b) $E_s = -0.7kT$, $L = 200$

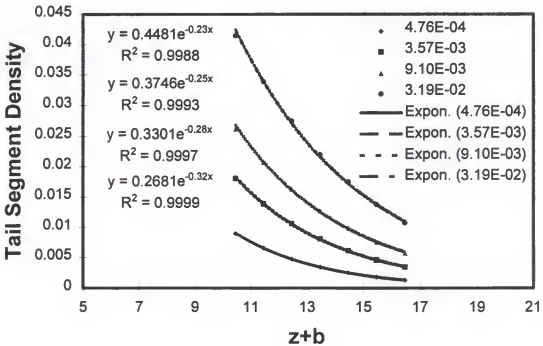


Figure 5.16. Tail segment density profile in the distal interface. The profiles show exponential decay.

REFERENCES

1. Homola, A.M., G.B. Street, C.M. Mate, *MRS Bulletin*, **XV**(3), 45 (1990).
2. Bird, R.B., R.C. Armstrong, O.Hassager, *Dynamics of Polymeric Liquids Vol. II Kinetic Theory*, Wiley Publ., New York (1977).
3. Denn, M.M., *Ann. Rev. Fluid Mech.*, **22**, 13 (1990).
4. Russell, W. B., D. A. Saville, W. R. Schowalter, *Colloidal Dispersions*, Cambridge New York Press, New York (1989),
5. Bitsanis, I., G. Hadziioannou, *J. Chem. Phys.*, **92**, 3827 (1990).
6. Bitsanis, I.A., C. Pan, *J. Chem. Phys.*, **99**, 5520 (1993).
7. Bitsanis, I., G. ten Brinke, *J. Chem. Phys.*, **99**, 3100 (1993).
8. Flory, P. J., *Principles of Polymer Chemistry*, Cornell University Press, Ithaca, NY (1971).
9. Fleer, G., M. Cohen-Stuart, J. Scheutjens, T. Cosgrove, B. Vincent, *Polymers at Interfaces*, Chapman and Hall, London, (1993).
10. Binder, K., editor, *Monte Carlo and Molecular Dynamics Simulations in Polymer Science*, Oxford University Press, New York, (1995).
11. des Cloizeaux J., G. Janink, *Polymers in Solution: Their Modeling and Structure*, Clarendon Press, Oxford (1990).
12. Fujita, H., *Polymer Solutions*, Elsevier Science Publishers, New York (1990).
13. Theodorou, D.N., *Macromolecules*, **21**, 1391 (1989).
14. Theodorou, D.N., *Macromolecules*, **22**, 4589 (1989).
15. Kumar, S.K., M. Vacatello, D.Y. Yoon, *J. Chem. Phys.*, **84**, 1922 (1988);
16. Kumar, S.K., M. Vacatello, D.Y. Yoon, *Macromolecules*, **23**, 2189 (1990).

17. Vacatello, M., D.Y. Yoon, B.C. Laskowski, *J. Chem. Phys.*, **89**, 779 (1990).
18. Scheutjens, J.M.H.M., G.J. Fleer, *J. Phys. Chem.*, **83**, 1619 (1979).
19. Scheutjens, J.M.H.M., G.J. Fleer, *J. Phys. Chem.*, **84**, 178 (1980).
20. Silberberg, A., *J. Coll. Inter. Sci.*, **90**, 86 (1981).
21. Silberberg, A., *J. Coll. Inter. Sci.*, **125**, 14 (1988).
22. Israelachvili, J.N., *Intermolecular and Surface Forces*, Academic Press, (1991).
23. Israelachvili, J.N., G.E. Adams, *J. Chem. Soc. Faraday Trans. I*, **74**, 975 (1978).
24. van Alsten, J., S. Granick, *Phys. Rev. Lett.*, **61**, 2570 (1988).
25. Israelachvili, J.N., P.M. McGuiggan, A.M. Homola, *Science*, **240**, 189 (1988).
26. Israelachvili, J.N., S.J. Kott, *J. Chem. Phys.*, **88**, 7162 (1988).
27. Homola, A.M., J.N. Israelachvili, M.L. Gee, P.M. McGuiggan, *J. Tribology*, **111**, 675 (1989).
28. Homola, A.M., H.V. Nguyen, G. Hadziioannou, *J. Chem. Phys.*, **94**, 2346 (1991).
29. Horn, R.G., J.N. Israelachvili, *Macromolecules*, **21**, 2836 (1988).
30. Montfort, J.P., G. Hadziioannou, *J. Chem. Phys.*, **88**, 7187 (1988).
31. Horn, R.G., S.J. Hirz, G. Hadziioannou, C.W. Frank, J.M. Catala, *J. Chem. Phys.*, **90**, 6767 (1989).
32. de Gennes, P.G., *Macromolecules*, **14**, 1637 (1981).
33. Obukhov, S.P., *Sov. Phys. JETP* **66**, 1125 (1987).
34. Rabe, J.P., S. Buchholz, *Phys. Rev. Lett.*, **66**, 2096 (1991).
35. Hentske, R., B.L. Schurmann, J.P. Rabe, *J. Chem. Phys.*, **92**, 6213 (1992).
36. Nikolov, A.D., D.T. Wasan, *J. Coll. Inter. Sci.*, **133**, 1 (1989).
37. Nikolov, A.D., D.T. Wasan, *J. Coll. Inter. Sci.*; **133**, 13 (1989).
38. Nikolov, A.D., D.T. Wasan, N.D. Denkov, P.A. Kralchesvsky, I.B. Ivanov, *Prog. Coll. Pol. Sci.*, **82**, 1 (1990).

39. Knudstrup, T.K., I.A. Bitsanis and G.B. Westermann-Clark, *Langmuir*, **11**, 893 (1995).
40. Peanasky, J., L.L. Cai, S. Granick, *Langmuir*, **10**, 3874 (1994).
41. Magda, J.J., M. Tirrell, H.T. Davis, *J. Chem. Phys.*, **83**, 1888 (1985).
42. Bitsanis, I., J.J. Magda, M. Tirrell, H.T. Davis, *J. Chem. Phys.*, **87**, 1733 (1987).
43. Bitsanis, I., S.A. Somers, H.T. Davis, M. Tirrell, *J. Chem. Phys.*, **93**, 3427 (1990).
44. Schoen, M., J.H. Cushman, D.J. Diestler, C.L. Rhykerd Jr., *J. Chem. Phys.*, **88** 1394 (1988).
45. Thompson, P.A., M.O. Robbins, *Phys. Rev. A.*, **41**, 6830 (1990).
46. Thompson, P.A., G.S. Grest, M.O. Robbins, *Phys. Rev. Lett.*, **68**, 3448 (1992).
47. Xia, T.K., J. Quyang, M.W. Ribarsky, U. Landman, *Phys. Rev. Lett.*, **69**, 1967 (1992).
48. Gupta, S., D.C. Koopman, G.B. Westermann-Clark, I.A. Bitsanis, *J. Chem. Phys.*, **100**, 8444 (1994).
49. Koopman, D.C., S. Gupta, R.K. Ballamudi, G.B. Westermann-Clark, I.A. Bitsanis, *Chem. Eng. Sci.*, **49**, 2907, (1994).
50. Ballamudi, R.K., I.A. Bitsanis, *Adsorption*, **2**, 69 (1996).
51. Ballamudi, R.K., I.A. Bitsanis, *J. Chem. Phys.*, **105**, 7774 (1996).
52. Granick, S., *Science*, **253**, 1374 (1991).
53. Ryckaert, J.P., A. Bellemans, *Faraday Discuss. Chem. Soc.*, **66**, 95 (1978).
54. Weber, T.A., *J. Chem. Phys.*, **69**, 2347 (1978)
55. Weber, T.A., *J. Chem. Phys.*, **70**, 4277 (1979).
56. Gupta, S., G.B. Westermann-Clark, I. Bitsanis, *J. Chem. Phys.*, **98**, 634 (1993).
57. Wang, Y., K. Hill, J.G. Harris, *J. Chem. Phys.*, **100**, 3276 (1994).
58. Chan, D.Y., R.G. Horn, *J. Chem. Phys.*, **83**, 5311 (1985).
59. Rubin, R., *J. Chem. Phys.*, **43**, 2392 (1965).
60. Rubin, R., *J. Res. Nat. Bur. Std.*, **70B**, 237 (1966).

61. Hoeve, C., S. Di Marzio, P. Peyser, *J. Chem. Phys.*, **42**, 2558 (1965).
62. Hoeve, C., *J. Polym. Sci.*, **C30**, 361 (1970).
63. Hoeve, C., *J. Polym. Sci.*, **C34**, I (1971).
64. Silberberg, A., *J. Chem. Phys.*, **46**, 1105 (1967).
65. Silberberg, A., *J. Chem. Phys.*, **48**, 2835 (1968).
66. Roe, R. J., *J. Chem. Phys.*, **60**, 4192 (1974).
67. Helfand, E., *J. Chem. Phys.*, **63**, 2192 (1974).
68. Helfand, E., *Macromolecules*, **9**, 307 (1976).
69. Weber, T. A., and E. Helfand, *Macromolecules*, **9**, 311 (1976).
70. de Gennes, P. G., *Scaling Concepts in Polymer Physics*, Cornell University Press, Ithaca.
71. Semenov, A.N., J. Bonet-Avalos, A. Johner, and J.F. Joanny, *Macromolecules*, **29** 1279 (1996).
72. Johner, A., J. Bonet-Avalos, C.C. van der Linden, A.N. Semenov, and J.F. Joanny, *Macromolecules*, **29**, 3629 (1996).
73. Semenov, A. N., and J.F. Joanny, *Europhys. Lett.*, **29**, 279 (1995).
74. Russell, T. P., *Material Sci. Repts.*, **5** 171, (1990)
75. Dijt, J.C., M.A. Cohen Stuart, J.E. Hofman, and G.J. Fleer, *Colloids Surfaces*, **51** 141 (1990).
76. Killmann E., and M. von Kuzenko, *Angewandte Makromol. Chem.*, **35** 39 (1974).
77. Tassin J.F., R.L. Siemens, W.T. Tang, G. Hadziioannou, J.D. Swalen, and B.A. Smith, *J. Phys. Chem.*, **93** 2106 (1989).
78. Creighton J.A., , C.G. Blatchford, and M.G. Albrecht, *J. Chem. Soc. Faraday Trans. II*, **75** 790 (1979)
79. Fu T.Z., and C.J. Durning, *Polymer Preprints ACS Div. Polym. Chem.*, **31** 519 (1990).
80. Cosgrove, T., T.G. Heath, K. Ryan, and T.L. Crowley, *Macromolecules*, **20** 2879 (1987).

81. Mathur, J. Adler, H. El-Shall, and B. Moudgil, "Conformation Studies of Adsorbed Polymer Using Atomic Force Microscopy", *Proc. Scanning 96, Foundation for Advances in Medicine and Science*, Monterey, CA. (1996).
82. Adler, S. Mathur, H. El-Shall, B. Moudgil, "Direct Measurement of Interparticle forces and their correlation with suspension stability, *Proc. 5th World Congress of AIChE*, San Diego, CA, July 14-18., 5, 504 (1996).
83. Adler, S. Mathur, H. El-Shall, B. Moudgil, "Effect of Polyelectrolyte on Rheological Behavior of Concentrated Aqueous Alumina Suspensions", *Proc. Of 5th World Congress of AIChE*, San Diego, CA, July 14-18., 5, 509 (1996).
84. Mate, M., M.R. Lorenz, and V.J. Novotny, Atomic Force Microscopy of polymeric liquid films, *J. Chem. Phys.*, **90** 7550 (1989).
85. Grest, G., and M. Murat in *Monte Carlo and Molecular Dynamics Simulations in Polymer Science*, Ed. K Binder, Oxford University Press, New York, (1995).
86. Milner, S.T., *Science*, **251** 905 (1991).
87. Halperin, M. Tirrell, and T.P. Lodge, *Adv. Polym. Sci.*, **100** 31 (1991).
88. Dobrynin, A.V., M. Rubinstein, S.P. Obukhov, *Macromolecules* **29** 2974 (1996).
89. Zheng, X., B.B. Sauer, J.G. Van Alsten, A. Schwarz, M.H. Rafailovich, J. Sokolov, and M. Rubinstein, *Phys. Rev. Lett.*, **74** 407 (1995).
90. Klein, J., and P.F. Luckham, *Macromolecules*, **17** 1041 (1984).
91. Chakraborty, A.K., and M. Tirrell, *MRS Bulletin*, **21** 28 (1996).
92. Binder, A. Milchev, and J. Baschnagel, *Ann. Rev. Mat. Sci.*, **26** 107 (1996).
93. Zajac, R., and A. Chakrabarti, *Phys. Rev. E*, **52** 6536 (1995).
94. Zajac, R., and A. Chakrabarti, *J. Chem. Phys.*, **104** 2418 (1996).
95. Lai, P.-Y., *J. Chem. Phys.*, **103** 5742 (1995).
96. Lai, P.-Y., *Phys. Rev. E.*, **53** 3819 (1996)
97. Metropolis, N., A. W. Rosenbluth, M. N. Rosenbluth, A. H. Teller, and E. Teller, *J. Chem. Phys.*, **21**, 1087 (1953).
98. Alder, B.J., T.E. Wainwright, *J. Chem. Phys.*, **27**, 1208 (1957)
99. Alder, B.J., T.E. Wainwright, *J. Chem. Phys.*, **31**, 459 (1959).

100. Alder, B.J. and T.E. Wainwright, *Phys. Rev.*, **127**, 359, (1962).
101. Rahman, A., *Phys. Rev.*, **136A**, 405 (1964).
102. Rahman, A., F. H. Stillinger, *J. Chem. Phys.*, **71**, 129 (1971).
103. Kremer, K., G.S. Grest, *J. Chem. Phys.*, **92**, 5057 (1990).
104. Lee, J.K., J.A. Barker, G.M. Pound, *J. Chem. Phys.*, **60**, 1976 (1974).
105. Chapela, G.A., G. Saville, S.M. Thompson, J.S. Rowlingson, *J. Chem. Soc. Faraday II*, **73**, 1133 (1977).
106. Frenkel, D., J.P. McTague, *A. Rev. Phys. Chem.*, **31**, 491 (1980).
107. Allen, M.P., D.J. Tildesley, *Computer Simulation of Liquids*, Oxford Publ., London (1987).
108. Ciccotti, G., D. Frenkel, and I. R., McDonald, *Simulation of Liquids and Solids: Molecular Dynamics and Monte Carlo Methods in Statistical Mechanics*, North Holland, New York (1987).
109. Roe, R.J., *Computer Simulation of Polymers*, Prentice Hall (1991).
110. Fishwick, P., *Simulation Model Design and Execution: Building Digital Worlds*, Prentice Hall, Englewood Cliffs, N.J. (1995)
111. Verlet, L., *Phys. Rev.*, **159**, 98 (1967).
112. Liu, Y., *Performance Analysis of Different Algorithms in Molecular Dynamics Simulation for Short Range and Long Range Interactions*, M.S. Thesis, University of Florida, Gainesville, (1995).
113. Catlow, C.R.A., S.C. Parker, M.P. Allen, *Computer Modelling of Fluids Polymers and Solids*, Kluwer Academic Publishers, London (1988).
114. Kolinski, A., J. Skolnick, R. Yaris, *J. Chem. Phys.*, **84**, 1922 (1986).
115. Reid, R.C., J.M. Prausnitz, B.E. Poling, *The Propertise of Gases and Liquids*, McGraw Hill (1977)
116. Toxvaerd, S., *J. Chem. Phys.*, **93**, 4290 (1990).
117. Padilla, P., S. Toxvaerd, *J. Chem. Phys.*, **94**, 5650 (1991).
118. Huang, D., Y. Cheng, K.A. Fichthorn, *J. Chem. Phys.*, **101**, (1994).
119. Helfand, E., *J. Chem. Phys.*, **71**, 5000 (1979)

120. Nicholson, D., N.G. Parsonage, *Computer Simulation and the Statistical Mechanics of Adsorption*, Academic Press, 1982.
121. McQuarrie, D.A., *Statistical Mechanics*, Harper and Row, New York (1973).
122. Mayer, J.E. and W.W. Wood, *J. Chem. Phys.*, **42**, 4268 (1965).
123. Hamza, A.V., R.J. Madix, *Surf. Sci.*, **179**, 25 (1987).
124. Andersen, H.C., M.P. Allen, A. Bellemans, J. Board, J.H.R. Clarke, M. Ferrario, J.M. Haile, S. Nose, J.V. Opheusden and J.P. Ryckaert. *Rapport d'activite scientifique du CECAM*, 82 (1984).
125. Evans, D.J., and G.P. Morriss, *Chem. Phys.*, **77**, 63 (1983).
126. Evans, D.J., and G.P. Morriss, *Comput. Phys. Rep.*, **1**, 297 (1984).
127. Andersen, H.C., *J. Chem. Phys.*, **72**, 2384 (1980).
128. Parrinello, M., and A. Rahman, *Phys. Rev. Lett.*, **45**, 1196 (1980).
129. Parrinello, M., and A. Rahman, *J. Appl. Phys.*, **52**, 7182 (1981).
130. Parrinello, M., and A. Rahman, *J. Chem. Phys.*, **76**, 2662 (1982).
131. Swope, W.C., H.C. Andersen, P.H. Berens, and K.R. Wilson, *J. Chem. Phys.*, **76**, 637 (1982).
132. Siepmann, J.I., and D. Frenkel, *J. Chem. Phys.*, **84**, 1922 (1986).
133. Rosenbluth, M.N., and A.W. Rosenbluth, *J. Chem. Phys.*, **23**, 356 (1955).

BIOGRAPHICAL SKETCH

Ravi Kiran Ballamudi graduated with a B.Tech. degree in chemical engineering from the Indian Institute of Technology, Madras in 1989. He worked with the Oil and Natural Gas Commission and RPG Enterprises for two years as an Assistant Engineer. He joined the Chemical Engineering Department at the University of Florida in Fall 1991, for graduate studies. In 1993 he obtained his Master's degree with special emphasis on process control. Subsequently, Ravi worked towards his Doctor of Philosophy degree with Professor Ioannis Bitsanis.

I certify that I have read this study and that in my opinion it conforms to acceptable standards of scholarly presentation and is fully adequate, in scope and quality, as a dissertation for degree of Doctor of Philosophy.



Ioannis A. Bitsanis, Chairman
Associate Professor of
Chemical Engineering

I certify that I have read this study and that in my opinion it conforms to acceptable standards of scholarly presentation and is fully adequate, in scope and quality, as a dissertation for degree of Doctor of Philosophy.



Paul A. Fishwick
Associate Professor of
Computer and Information
Sciences and Engineering

I certify that I have read this study and that in my opinion it conforms to acceptable standards of scholarly presentation and is fully adequate, in scope and quality, as a dissertation for degree of Doctor of Philosophy.



Lewis Johns, Jr.
Professor of Chemical
Engineering

I certify that I have read this study and that in my opinion it conforms to acceptable standards of scholarly presentation and is fully adequate, in scope and quality, as a dissertation for degree of Doctor of Philosophy.



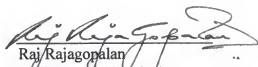
Chang-Won Park
Associate Professor of
Chemical Engineering

I certify that I have read this study and that in my opinion it conforms to acceptable standards of scholarly presentation and is fully adequate, in scope and quality, as a dissertation for degree of Doctor of Philosophy.



Sergei Obukhov
Associate Professor of Physics

I certify that I have read this study and that in my opinion it conforms to acceptable standards of scholarly presentation and is fully adequate, in scope and quality, as a dissertation for degree of Doctor of Philosophy.



Raj/Rajagopalan
Professor of Chemical
Engineering

This dissertation was presented to the Graduate Faculty of the College of Engineering and to the Graduate School and was accepted as partial fulfillment of the requirements for the degree of Doctor of Philosophy.

May 1997



Winfred M. Phillips
Dean, College of Engineering

Karen A. Holbrook
Dean, Graduate School